UNIVERSITÉ DE SHERBROOKE

Faculté de génie
Département de génie chimique

Synthèse de nanoparticules de carbure de fer dans un réacteur à plasma inductif

Synthesis of Iron Carbide Nanoparticles in an Induction Plasma Reactor

Mémoire de maîtrise ès sciences appliquées
Spécialité : génie chimique

Composition du jury

François Gitzhofer
Nicolas Abatzoglou
Ajay K. Dalai
Denis Gravelle

Roham Eslahpazir Esfandabadi

Sherbrooke (Québec), CANADA January 2009

Your file Votre référence
ISBN: 978-0-494-49497-4
Our file Notre référence
ISBN: 978-0-494-49497-4

Résumé

Dans cette étude, les nanoparticles de carbure de fer ont été synthétisées dans un réacteur à plasma inductif. Dans ce travail nous nous sommes concentrés sur les applications du carbure de fer comme catalyseur de la réaction Fischer-Tropsch. Il y a beaucoup d'applications pour le carbure de fer en recherche et dans l'industrie, comme par exemple dans les ferrofluides, l'enregistrement magnétique et les biocapteurs.

Deux différentes méthodes d'injection ont été utilisées dans ce projet. L'injection de suspension avec l'avantage d'injecter des précurseurs hétérogènes, et l'injection de solide pour introduire les précurseurs avec tout ratio molaire désiré.

L'influence de différents facteurs a été étudiée (puissance, débit d'injection, position de la sonde, taille de particules et ratio molaire des réactifs) sur la composition chimique ainsi que la morphologie des particules produites. Différentes méthodes de caractérisation comme, la diffraction des rayons X (DRX), la microscopie électronique à balayage (MEB), la microscopie électronique à transmission (MET) , l'analyse thermogravimétrique, et l'analyse de la surface spécifique par méthode BET ont été utilisées.

Les résultats de DRX ont montré que les particules produites contiennent environs 50% massique de carbure de fer et que les autres composants produits sont l'austénite, le graphite et le fer pur. Les images de MEB et MET ont révélé que les particules nanométriques avec des diamètres entre 10 et 50 nm ont été produites à coté de plus grosses particules de diamètre entre 1 et 5 μm. Les images de MET en haute résolution ont montré que les particules nanométriques ont une structure «noyau-coquille» et qu'elles sont enrobées avec une couche de carbone amorphe et graphitique.

Une nouvelle technique de collecte de nanopoudre produite a aussi été développée afin de collecter des poudres dans un liquide inerte. Le but de cette méthode est de minimiser la dispersion des nanoparticules dans l'air et de les protéger contre l'oxydation instantanée.

Mots-clés: plasma inductif, nanoparticules, carbure de fer, injection de suspension, réaction Fischer-Tropsch, catalyseur

Abstract

In this study nanometric iron carbide particles were produced by using an induction thermal plasma reactor. There are several applications for iron carbide particles in research and industry, such as in ferrofluids, magnetic recording and biosensors. We are focused in this project on its application as catalyst for Fischer-Tropsch reaction.

Two different injection methods were used in this study. Suspension injection was used because of its capability to inject heterogeneous precursors, and solid injection was used to inject reactants with any desired molar ratio.

The effect of several process parameters was investigated (plate power, injection rate, probe position, particle size and reactant ratio) and composition and morphology of produced powder were characterized using several characterization techniques including X-ray Diffraction (XRD), Scanning Electron Microscopy (SEM), Transmission Electron Microscopy (TEM), Thermogravimetric Analysis (TGA), and specific surface area measurement using BET method.

XRD results showed that the produced powder has about 50% of iron carbide alongside other phases such as pure iron, austenite and graphite. SEM and TEM images revealed that nanometric particles with a diameter between 10-50 nm were produced alongside larger particles with diameter between 1 to 3 μm. High resolution TEM images showed that the produced nanometric particles have a core-shell structure and that they are embedded in an amorphous carbon.

A new method has also been developed to collect the produced nanopowder in a liquid in order to minimize nanoparticle dispersion into the air, and protect pyrophoric nanoparticles from air exposure.

Keywords: Induction thermal plasma, nanoparticle, iron carbide, suspension injection, Fischer-Tropsch reaction, catalyst

Acknowledgment

My first thanks go to my supervisors Prof. François Gitzhofer and Prof. Nicolas Abatzoglou who helped me during realization of this project. Without their scientific advises, patience and encouragement this project could have never been accomplished.

All members of Plasma Technologies Research Centre (CREPE) especially Mr. Francis Barrette with his technical support have helped me in this project. Contributions of all my group mates in Groupe de Recherche en Énergie et Environnement (GREEN) with their supports and advises are gratefully acknowledged.

I would like to thank the Natural Science and Engineering Research Council (NSERC) of Canada, Natural resources of Canada, and Enerkem Company for their financial supports.

Finally and specially, I want to thank my wife, Nafiseh, for her encouragement and patience which was a source of love and positive energy for me.

Table of Content

1. INTRODUCTION 1
   1.1. Overview 1
   1.2. Iron carbide Applications 2
      1.2.1. Miscellaneous applications 2
      1.2.2. Fischer-Tropsch reaction 3
   1.3. Nanometric iron carbide synthesis techniques 5
   1.4. Problem description and thesis objectives 6
   1.5. Structure of the thesis 7
2. LITERATURE REVIEW 9
   2.1. Overview 9
   2.2. Chemical vapor condensation (CVC) 9
   2.3. Chemical vapor deposition (CVD) 10
   2.4. Laser pyrolysis 12
   2.5. Arc discharge 13
   2.6. Thermal plasma 17
      2.6.1. The plasma state 17
      2.6.2. Thermodynamic and transport properties 18
      2.6.3. Generation of radio frequency (RF) plasma 23
      2.6.4. Nanoparticles synthesis by R.F plasma 24
3. EXPERIMENTAL METHODS 27
   3.1. Experimental set up 27
   3.2. Injection techniques 31
   3.3. Wet collection method 33
   3.4. Characterization techniques 36
   3.5. Operating conditions 39
   3.6. Experimental design 41
4. RESULTS AND DISCUSSIONS 42
   4.1. Overview and objectives 42
   4.2. Suspension Injection: Preliminary results 42

4.2.1. Objectives 42
4.2.2. Thermodynamic analysis 42
4.2.3. Preparation 45
4.2.4. Oxygen containing precursors 46
4.2.5. Hydrocarbon precursor 51
4.2.6. Discussions 53
4.3. Suspension injection: statistical analysis 55
4.3.1. Objectives 55
4.3.2. Determination of 2^3 design levels 55
4.3.3. Characterization 57
4.3.4. Statistical analysis 64
4.3.5. Discussions 66
4.4. Solid injection technique 68
4.4.1. Objectives 68
4.4.2. Operational conditions and results 69
4.4.3. Characterization 72
4.4.4. Discussions 77
CONCLUSION 80
References 83

List of Figures

Figure 2.1 Laser pyrolysis system for nanoparticle production 12
Figure 2.2 Classic arc discharge reactor 14
Figure 2.3 X-ray diffraction spectra of (a) Fe(C), (b) Co(C) and (c) Fe–Co(C) nanocapsules 15
Figure 2.4 HRTEM images showing the shell–core structure of Fe(C) 16
Figure 2.5 Encapsulated iron nanoparticles 17
Figure 2.6 Typical range of electron temperature and electron density for thermal and cold plasma 18
Figure 2.7 Composition of (a) argon, (b) nitrogen, plasma as a function of temperature 19
Figure 2.8 Specific enthalpy of some monatomic and molecular gases as a function of temperature 20
Figure 2.9 Thermal conductivity of H_2/Ar mixture as a function of temperature 21
Figure 2.10 Axial profiles of the (a) velocity, (b) temperature and (c) injected gas concentration 22
Figure 2.11 Axial profiles of the (a) viscosity, (b) thermal conductivity and (c) mass diffusivity 23
Figure 2.12 Schematic view of dual-RF torch 25
Figure 2.13 TEM images of Fe Si-C powder 26
Figure 3.1 Experimental set up 28
Figure 3.2 Plasma torch 29
Figure 3.3 Suspension injection probe 30
Figure 3.4 SEM images of initial iron particle 31
Figure 3.5 Two schematic view of liquid injection flange 33
Figure 3.6 Liquid film formation during wet collection 34
Figure 4.1 Thermodynamic equilibrium of the butanol/glycerol/iron system 43
Figure 4.2 Thermodynamic equilibrium of mineral oil/iron the system 44
Figure 4.3 XRD result of OL-1 47
Figure 4.4 SEM images of test OL-1 (a) Secondary electron detector (b) backscattered electron detector 49
Figure 4.5 SEM images of round micrometric balls (test OL-2) 50

Figure 4.6 Peaks of OL-3 51
Figure 4.7 XRD results of produced iron carbide powder 52
Figure 4.8 TEM images of test S-5 60
Figure 4.9 Graphite layers 61
Figure 4.10 HRTEM image of iron carbide nanoparticle 62
Figure 4.11 TGA result of pure iron 63
Figure 4.12 TGA of test S-5 64
Figure 4.13 Effect of injected iron particle diameter on conversion 70
Figure 4.14 XRD spectrum of test P-1 72
Figure 4.15 TEM image of test P-4 73
Figure 4.16 TEM image of a particle test P-4 74
Figure 4.17 HRTEM image of particle shown in Figure 4-14 75
Figure 4.18 TGA analysis, ... 76

List of Tables

Table 1.1 Different applications of iron carbide nanoparticles 3
Table 3.1 List of characterization methods and their applications 36
Table 3.2 Preliminary tests experimental conditions 39
Table 3.3 Experimental parameters for factorial design runs 40
Table 3.4 Solid injection experimental conditions 40
Table 3.5 2^3 statistical factorial design 41
Table 4.1 Experimental condition, oxygenate precursor 47
Table 4.2 Experimental condition of ML tests 52
Table 4.3 Levels and parameters for factorial design 56
Table 4.4 2^3 factorial design 57
Table 4.5 XRD semi-quantitative analysis 58
Table 4.6 ANOVA table 65
Table 4.7 Operational condition, powder injection mode 69

1. INTRODUCTION

1.1. Overview

Nanoparticles are particles with size between 1 to 100 nm. These particles have special characteristics which make them different from bulk materials. These special properties give nanoparticles certain advantages, because of their new physical, chemical or biological properties and their huge surface to mass ratio (Roco, M.C., 1999).

Several processes for synthesis of nanoparticles have been developed based on nature and desired characteristics of targeted materials. Purity of produced nanoparticles and narrow size distribution are two important concerns in all methods beside other important factors like the stability of nanoparticles and the productivity of method. Scale-up problems and cost of final product should be considered for commercial production of nanoparticles.

Thermal plasma has various applications like deposition of corrosion-, temperature-, and abrasion-resistant coatings, densification, spheroidization, waste destruction and nanoparticle synthesis (Pfender, E., 1999); (Smith, R.W. et al., 1989b). Several efforts have been done to commercialize these applications and some of them have been used for industrial fabrications: for example, deposition of diamonds and dense ceramics or superconducting films (Pfender, E., 1999) and production of TiO_2 pigments (Boulos, M.I., 1985).

In next sections of this introduction some of the applications of iron carbide nanoparticles will be introduced. A separate section is dedicated to the application of iron carbide as catalyst for Fischer-Tropsch Synthesis (FTS) which is the targeted application for powder produced in this study. Different synthesis techniques will be briefly mentioned in the following section. Problem description and main objectives of thesis is the subject of section 1.4 and this introduction terminates with a description of the thesis' main chapters.

1.2. Iron carbide Applications

1.2.1. Miscellaneous applications

Several applications for iron carbide nanoparticles are reported in the literature. A list of these applications is shown in Table 1.1. Iron carbide particles produced by different methods are usually covered with a graphitic or amorphous carbon layer. This special structure gives them wide applications because it prevents iron carbide particles from oxidation. This nonmagnetic layer also enhances the magnetic stability of nanosized particles by reducing their random flipping of the magnetic moment occurring by thermal fluctuations (Sajitha, E.P. et al., 2004).

Presence of carbon layer on the iron carbide surface made iron carbide nanoparticles compatible with organic media (Song, H. et al., 2003). The application of metal particles encapsulated in carbon layer is in biosensors and drug delivery fields.

In nanocatalysts, the diameter of the particles plays an important role and it affects both activity and selectivity of nanocatalysts. The number of active sites on the surface of particle per catalyst volume increases as the size of particle decreases. This feature makes the nanocatalysts more active and more economic compare to conventional catalysts. Moreover, the surface structure of particles is different from that of a bulk material and this causes differences in selectivity of produced materials (Kameyama, T. et al., 1993a).

Table 1.1 Different applications of iron carbide nanoparticles

Applications related to magnetic properties:	
magnetic recording	(Lee, D.W. et al., 2008)
magnetic fluids	(Lee, D.W. et al., 2008)
magnetic refrigerants	(Lee, D.W. et al., 2008)
magnetic toner	(Kim, J.H. et al., 2007)
magnetic resonance imaging	(Kim, J.H. et al., 2007)
Biomedical :	
biosensors	(Song, H. et al., 2003)
drug delivery	(Song, H. et al., 2003)
Catalyst	(Cheng, J.P. et al., 2008)

1.2.2. Fischer-Tropsch reaction

The Fischer-Tropsch Synthesis (FTS) has about 70 years of lively history (Schulz, H., 1999). During 1930's and 1940's early catalyst development and commercial applications took place in Germany (Schulz, H., 1999). Today it is considered as a potential process for producing clean transportation fuels and chemical productions. Hans Schulz has reported three major advantages for FTS in his review: (i) converting natural gas to liquid product to facilitate its transportation, (ii) reduce CO_2 release and increase energy saving by converting flare gases to liquids, (iii) producing clean diesel from residual heavy oils (Schulz, H., 1999). We can also add the potential of FTS for producing alternative fuels from coal or natural gas when the price of crude oil is more than 16-18 $ per barrel (Dry, M.E., 2002).

Four metals are known to be active for FT synthesis. Ruthenium is used only for laboratory scale experiments because of its high price. Nickel is very active for methane formation so it has no commercial applications. Cobalt and Iron are two metals used for industrial catalyst production (Schulz, H., 1999). It is practical to add promoters to these two metals to improve their structural and chemical properties.

The chemistry of FTS and side reactions can be described by following reactions (Bartholomew, C.H., 1990)

$$CO + 3H_2 \rightarrow CH_4 + H_2O \quad (1.1)$$

$$CO + 2H_2 \rightarrow -CH_2- + H_2O \quad (1.2)$$

$$CO + H_2O \rightarrow CO_2 + H_2 \quad (1.3)$$

$$2CO \rightarrow C + C_2O \quad (1.4)$$

Reaction (1.1) is the formation of methane. Reaction (1.2) shows the synthesis of hydrocarbons heavier than methane, reaction (1.3) shows the Water Gas Shift (WGS) reaction, and (1.4) is known as the Boudouard reaction and shows carbon deposition on catalyst surface.

Methane formation is not a desired reaction because the goal of the process is to produce heavy hydrocarbons. Reaction (1.2) is the main reaction which produces molecules with a polymer like structure with –CH2- as monomer. Iron based catalyst are very active for WGS reaction and this reaction is in its equilibrium state when the temperature of reactor is high (330 to 360°C) (Davis, B.H., 2003). Reaction (1.4) shows the formation of carbonaceous layer on catalyst surface which is one of the mechanisms for catalyst deactivation (Jäger, C. et al., 2006) .

FTS operational condition is divided into two main categories: Low Temperature Fischer-Tropsch (LTFT) and High Temperature Fischer-Tropsch (HTFT). The first category represents reaction at temperature range from 225 to 260°C (Dry, M.E., 1996) and it is suitable for heavy hydrocarbons production like diesel and wax. The HTFT is used for light

hydrocarbon production like gasoline and light olefins. Temperature range for HTFT is between 330 and 360°C (Dry, M.E., 1996).

1.3. Nanometric iron carbide synthesis techniques

Up to now, several techniques have been employed to synthesize iron carbide. These techniques can be divided into two groups: gas phase reactions and solid-gas reactions. Laser pyrolysis, Chemical Vapor Condensation (CVC) and arc discharge are methods in which iron carbide is formed by reaction with gaseous precursors.

In laser pyrolysis method iron pentacarbonyl is used as iron precursor. Iron pentacarbonyl has a low boiling point (103°C) and its decomposition begins at about 300°C (Jager, B. et al., 1995). In this method a laser beam produced by CO_2 gas is focused in a spot where iron pentacarbonyl and a hydrocarbon gas as carbon donor are injected by means of a concentric nozzle. A third gas is used in this method to absorb laser energy and transform this energy to reactant. This gas is called sensitizer and for CO_2 laser ethylene molecule can absorb energy by resonant absorption of photons (Alexandrescu, R. et al., 2005).

In CVC method iron pentacarbonyl decomposes in a furnace in temperatures around 800°C and reacts with a carbon donor gas, e.g. methane, to produce iron carbide in gas phase. Produced materials will be condensed and deposited on the wall of collection chamber (Lee, D.W. et al., 2008).

In order to produce iron carbide with an arc discharge method, silicon carbide and iron powder is pressed into a cylinder and the two are used as anode. Discharge takes place under argon gas using a tungsten electrode as cathode. Silicon carbide and iron particles evaporate and form iron carbide and Fe-C-Si alloy (Si, P.Z. et al., 2005).

In a typical CVD method, iron particles are used as catalyst for hydrocarbon decomposition on the surface of particles and consequently the formation of iron carbide takes place. Sajitha *et al* have used iron pentacarbonyl as an iron precursor. In this case the iron particles produced from prior decomposition of iron pentacarbonyl (Sajitha, E.P. et al., 2004).

Simple carburization of pure iron or iron oxide is also possible to produce iron carbide (Arabczyk, W. et al., 2004).

1.4. Problem description and thesis objectives

Several researchers tried to find the most active iron phase for Fischer-Tropsch synthesis. Presence of both oxidant (H_2O and CO_2) and reductant (CO and H_2) gases in the reactor and phase evolution of catalyst during the reaction were the cause of problems for these researchers. Bukur *et al* reported in their article that the iron atoms at the surface of catalyst with different bulk phases are the active sites for FTS (Bukur, D.B. et al., 1999). Meanwhile, other researchers find a good correlation between bulk iron carbide formation and the activity of these catalysts and they argued that the iron carbide at the surface of these catalysts provides active sites for this reaction. Activity of surface iron carbide is also reported in recent article of Davis *et al* (Davis, B.H., In press).

Different reaction conditions and pretreatments can be the source of these contradictions. In all above mentioned studies the catalyst particles are used in reactor after activation periods to convert iron oxide to metallic iron or iron carbide.

In this work nanometric iron carbide was produced in order to eliminate the activation step for the FTS catalyst. The nanometric size of particles also provides a large number of active sites on the surface of catalyst. Surface structure and bulk of nanoparticles are also identical because of the small size of nanoparticles.

Another advantage of using a nanocatalyst is in the elimination of the porous structure. In LTFT the formation of liquid hydrocarbons will produce an additional two limiting steps for the overall reaction: first when reactants have to diffuse into the liquid phase to reach the catalyst surface, and second when the gaseous products want to leave catalyst surface to be replaced by new reactants. When catalyst pores are filled with liquid this procedure might reduce the overall reaction rate. These pores are also prone to be blocked in harsh reaction conditions hence reducing the specific surface of the catalyst (Li, S. et al., 2002).

An induction plasma reactor is used in this study because of its capability for nanoparticle production and also its high productivity. From the author's knowledge, none of any previous researchers had produced doped iron carbide nanoparticles. The feasibility of adding promoters to iron carbide will also be examined in this work.

Previous studies in nanoparticle production by induction plasma reactor shows that process parameters may influence the structure and the morphology of produced particles (Guo, J. et al., 1997); (Soucy, G. et al., 1995). A factorial design has been implemented to investigate possible effects of process factors like plate power, injection flow rate and injection probe position.

In this work the dispersion of nanoparticles during collection causes students and technicians to be exposed to produced nanomaterials. A new collection technique is developed to collect nanoparticles by means of a liquid film. Another advantage of this new developed technique is in the prevention of pyrophoric nanoparticle exposure to oxygen in the air.

More specifically, the objectives of this thesis are to:

- Produce nanometric iron carbide particles
- Investigate the role of production parameters in structure and morphology of produced particles
- Compare liquid injection and solid injection of precursor
- Develop a new method for nanoparticle collection

1.5. Structure of the thesis

This thesis consists of 5 chapters. The first and second chapters are an introduction and literature review. In the literature review section, different methods for iron carbide nanoparticle synthesis are reviewed and in each case, the main parameters and their influence on the final product are reported.

The third chapter covers the description of the experimental setup and of the characterization methods used in this study. First a complete description of the system used for nanoparticle production is presented. Later, a brief description of the scientific principles of each characterization techniques is presented, followed by a range of parameters used in each technique. A detailed description of the newly developed system for wet collection is presented in the final section.

The fourth chapter focuses on the effect of different parameters in the conversion extent of iron to iron carbide. Characteristics of powders obtained when we applied liquid injection

method are also reported in this chapter. A comparison between liquid and solid injection methods is reported in this chapter.

Finally some conclusions are drawn on the basis of obtained results and some suggestions for future work are mentioned.

2. LITERATURE REVIEW

2.1. Overview

In this literature review, various methods of iron carbide production are presented. The objective of this section is to study the important factors in iron carbide synthesis such as residence time, temperature, pressure and chemical nature of precursors. Methods for production of coarse particles are not covered in this section. Morphology and chemical composition of produced powder are reviewed, and the plasma technology is discussed in detail.

2.2. Chemical vapor condensation (CVC)

In this method iron-pentacarbonyl is used because of its low boiling point. Lee *et al* in their article described CVC method as follows (Lee, D.W. et al., 2008):

Iron-pentacarbonyl is evaporated in a bubbling unit at 150°C and the vapor is mixed with high purity methane gas. The gas mixture then is introduced into a plug flow reactor with a temperature and pressure range between 500-800°C and 1.33 to 101 kPa. The precursors decompose in these conditions and the produced iron carbide particles were deposited on the wall of the collection chamber. Subsequently, the produced particles were passivated for 2 h with a gas mixture of Ar and O_2.

The same experimental technique as above was presented by Wang *et al* in their article (Wang, Z.H. et al., 2003). The main difference is that Wang *et al* have used CO instead of CH_4 as carbon donor precursor.

Effect of Temperature

When CO is used as the precursor; Wang *et al* in the same article investigated the effect of temperature on chemical composition and crystalline structure of produced particles. In their study XRD results showed that at 400°C only b.c.c (body centered cubic) iron is produced while increasing temperature to 600°C results in the formation of Fe_3C. At 700°C pure iron carbide is produced and further temperature increase to 1100°C results in formation of b.c.c Fe, f.c.c (face centered cubic) Fe and Fe_3C.

When CH_4 is used as the precursor; Lee et al also used their XRD results to study the formation of different phases in the produced powders (Lee, D.W. et al., 2008). They found that at 500°C no iron carbide is produced while at 650°C, α-Fe and Fe_3C coexist and at 800°C only Fe_3C is detected by XRD. They concluded that at 500°C there was not enough thermal energy for the formation of iron carbide.

Effect of pressure and residence time

Lee *et al* in the same article changed the pressure of plug flow reactor (furnace) to investigate the effect of the pressure and consequently the particle residence time on the final product. The results showed that at low pressure (1.3 Pa) the powder contained only α-Fe. Based on their estimation, at this pressure the residence time was about some millisecond. However, when they increased the pressure to 101 kPa they obtained iron carbide in their powder. At this pressure the estimated residence time was some seconds.

2.3. Chemical vapor deposition (CVD)

There are two types of vapor deposition; (i) physical vapor deposition, (ii) chemical vapor deposition. The difference between these two processes is that the second one involves a chemical reaction between precursors.

In CVD method, at least one solid precursor was placed in a quartz tube heated by an electric coil or placed in an autoclave. The precursor was heated to desired temperature in a controlled atmosphere and the produced powder was collected after the reaction's completion. Ferrocene was used as metallic precursor in the furnace (Qiu, J. et al., 2006); (Sajitha, E.P. et al., 2004) while different carbon donor precursors were used to produce iron carbide. Qui *et al* used a sort of pipe gas derived from coal because of its reasonable coast (Qiu, J. et al., 2006). Sajitha *et al* in their study used maleic anhydride ($C_4H_2O_3$) (Sajitha, E.P. et al., 2004) and Song *et al* used 1,2,3,4-therimethylbenzene (durene) to provide carbon for iron carbide formation (Song, H. et al., 2003). The common property of these precursors is in their evaporation and decomposition at low temperature (below 1000° C). In addition, it is

worthwhile to note that ferrocene can provide both iron and carbon after its decomposition: hence it can be used alone for iron carbide synthesis (Sano, N. et al., 2003).

Effect of Fe/C

Sajitha *et al* in their study used different ratios of maleic anhydride to iron in order to investigate the effect of Fe/C ratio on the morphology and composition of the produced powder (Sajitha, E.P. et al., 2004). XRD results of the prepared sample showed that as the molecular weight of iron increases from 5 to 50% the (002) peak of graphite becomes more intense and peaks of different iron carbide phases also appear on the XRD spectra. They concluded that an intermediate compound of iron carbide was formed and then decomposed to form graphitized carbon matrix with iron carbide crystals embedded in it.

Morphology and size

Different precursors and synthesis techniques result in differences in morphology and size of the produced particles. Sajitha *et al* used a quartz tube with one end closed and placed maleic anhydride and ferrocene in the closed end and heated the tube up to 900° C (Sajitha, E.P. et al., 2004). The exhaust gases cooled in an external bladder and the produced powder was deposited on its wall. The produced powder had a dark core and a bright shell as revealed by TEM. SAED results showed only graphite characteristic rings corresponding to (002) and (100) planes.

Song *et al* in their study placed durene and ferrocene in an autoclave and heated it up to 540° C (Song, H. et al., 2003). TEM results showed formation of about 20 nm particles embedded in an amorphous carbon while HRTEM showed that the carbon layer near iron carbide particles has a graphite structure with interlayer spacing of 0.336 nm which corresponds to graphite (002) plane. The carbon structure away from iron carbide core has an amorphous structure hence they concluded that these carbons were formed as the result of durene decomposition without metal interference.

2.4. Laser pyrolysis

This method was first used by Fiato and Rice, two Exxon researchers for pure iron carbide production (Xiang-Xin Bi et al., 1993). Other researchers did further research to improve this procedure and to modify it for production of different iron carbide phases.

In this method two concentric nozzles are placed in a sealed chamber and a CO_2 laser beam is crossing the gas stream in the center of this reaction cell (Jäger, C. et al., 2006). The reactive gases, usually iron-pentacarbonyl and acetylene, are admitted through the inner nozzle and each of them is entrained by the sensitizer. The sensitizer is the gas which is used to absorb the energy of the laser and to transfer it to reactive gases by collision. Argon is injected from the outer nozzle to confine the gas streams and to nucleate the particles. The nucleated particles are entrained by the gas stream to the cell's exit where they are collected in a trap. The experimental set-up for production of TiO2 is presented in Figure 2.1 (Alexandrescu, R. et al., 2004).

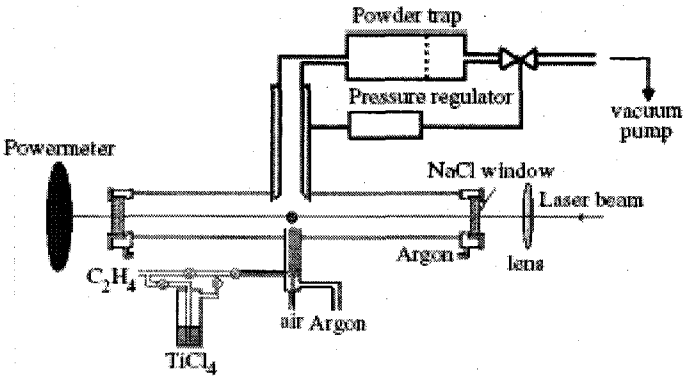

Figure 2.1 Laser pyrolysis system for nanoparticle production (Alexandrescu, R. et al., 2004)

Effect of Temperature

There are two ways to increase the temperature of the reactor, first to increase the power of the laser and second to increase the flow rate of the sensitizer (Alexandrescu, R. et al., 2005). Both of these changes resulted in the formation of smaller particles. Alexanderescu et al in the same article showed that by increasing the flow rate of C_2H_4 from 30 to 40 sccm (standard cubic centimeter per minute) when the pressure of the reactor is constant at 500

mbar, the mean diameter of particles decreases from 8 to 6 nm. In the other experiment in the same study they increased the laser power from 80 to 100 W and they found that the mean diameter further decreased to 4-5 nm.

Effect of different gas phase precursor

Alexanderescu *et al* in another article studied the effect of acetylene and toluene as a carbon donor gas (Alexandrescu, R. et al., 2007). The other conditions were held constant during two experiments. They reported that the powder prepared by toluene has a higher portion of iron carbide.

The mechanism of iron carbide formation was also discussed in the same paper. First the iron-pentacarbonyl decomposes due to its low dissociation energy. This dissociation proceeds until the formation of iron particles and CO liberation occurs. The produced iron particles then decompose hydrocarbon as a catalyst and the produced free carbon atoms react with iron to form iron carbide.

2.5. Arc discharge

This method was first developed for production of fullerene and single- or multi-walled carbon nanotubes. Farhat *et al* in their review described the basics of arc process for production of fullerene, single-walled carbon nanotubes (SWCNT) and multi-walled carbon nanotubes (MWCNT) (Farhat, S. et al., 2006). A summary of their description is presented here.

Most of laboratory scale reactors consist of a water-cooled reactor chamber with two graphite electrodes as shown in Figure 2.2. The electrode gap can be adjusted during the process by means of an optical window placed in front of the plasma zone. In order to produce fullerene and MWCNT the anode is made of pure graphite while for SWCNT the production anode consists of a graphite rod filled with catalysts like Co, Fe or Ni. Once the process is ended, a ventilation system is used to avoid dispersion of soot into the room. The cathode is made of graphite or Cu. During the process, it is essential to keep the distance

between electrodes constant to produce a stable discharge and a constant rate of anode erosion.

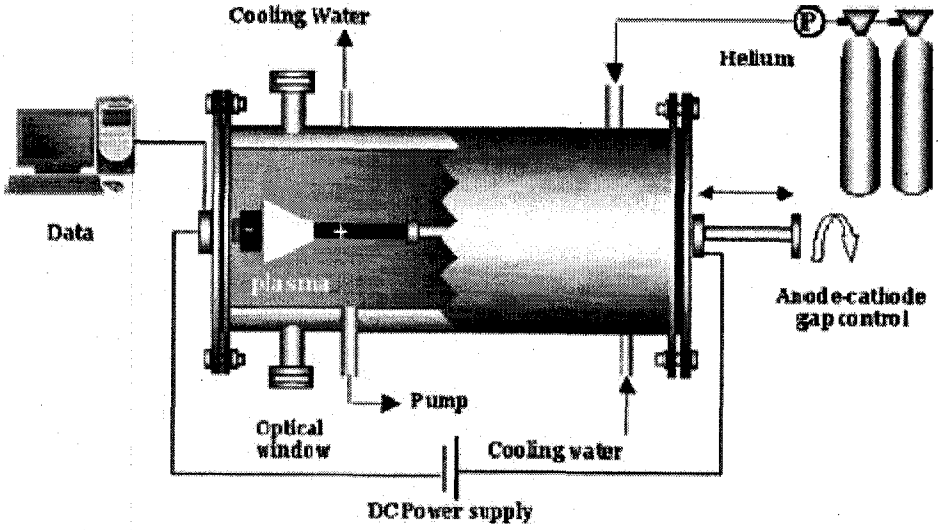

Figure 2.2 Classic arc discharge reactor (Farhat, S. et al., 2006)

Anode and cathode are in contact in the beginning of the process to ignite the plasma. The temperature of the contact point increases until the anode material evaporation begins. Then by adjusting the anode-cathode gap the burning rate of the anode was controlled.

Carbon species and catalysts were deposited on the end of the cooled cathode while soot was removed by free convection and was deposited on the wall of the reactor.

Some modification in the above method has been done by other researchers to produce iron carbide or carbon coated iron particles instead of nanotubes or fullerenes. Si *et al* in their study used 10 g of SiC and 37.5 g of commercial iron for anode (Si, P.Z. et al., 2005). They pressed these powders to form a cylindrical anode and they used tungsten as a cathode. The arc discharge was performed under Ar flow and the discharge current was 120-160 A. XRD results showed formation of Fe-Si-C alloy and also α-Fe peak but no peak corresponding to SiC was detected. They concluded that all SiC was decomposed and that the reaction between Fe and SiC was very rapid. The produced particles had a core-shell structure revealed by TEM and a size distribution between 10 to 60 nm. They also examined the stability of their powder by oxidizing it in air for 3 hr at 630K. The formation of iron oxide phase indicated that all the particles were not completely coated by a protective carbon layer.

Zhang *et al* tried to synthesize Fe-Co(C) nanocapsules by using the same method (Zhang, Z.D. et al., 2001). The modification they applied to classic arc method was to use $Fe_{70}Co_{30}$ alloy as anode and graphite as cathode. They also mixed He with 30% of CH_4 and used it as discharge gas. They reported that when voltage reached 20-30 V the Fe-Co alloy began to evaporate while CH_4 was decomposed into C and H.

They did three experiences to change the anode composition from pure iron to pure cobalt and finally to Fe-Co alloy. In the first experience the result of XRD showed the formation of γ-Fe (Austenite), α-Fe and iron carbide (Figure 2.3). Pure cobalt resulted in the formation of only pure cobalt particles while XRD detected only iron phase when they used iron-cobalt alloy.

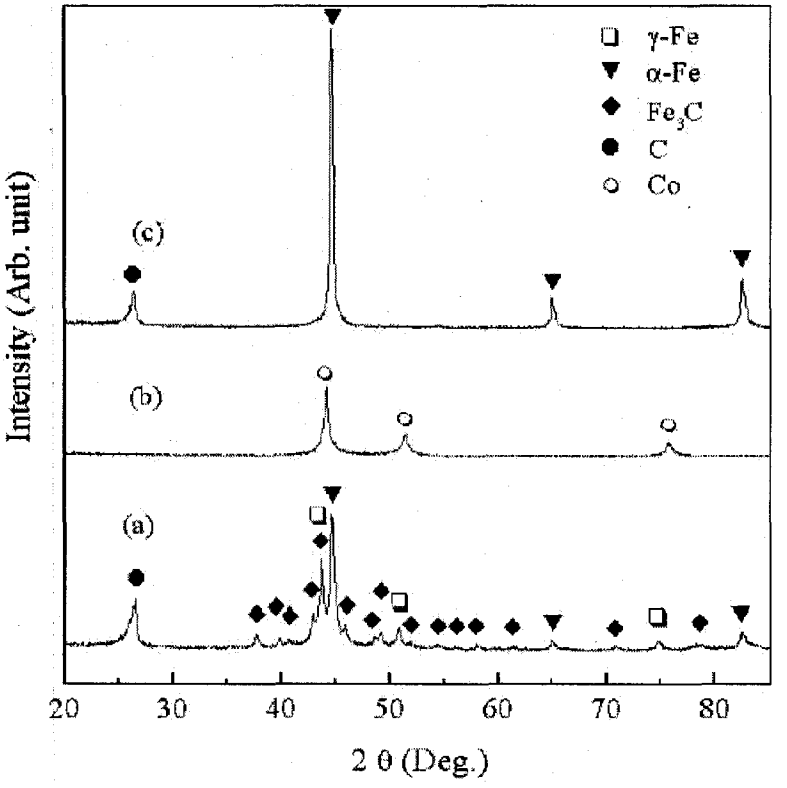

Figure 2.3 X-ray diffraction spectra of (a) Fe(C), (b) Co(C) and (c) Fe–Co(C) nanocapsules (Zhang, Z.D. et al., 2001)

They used HRTEM to show the core-shell structure of produced particles. In Figure 2.4 the inner dark core is the iron particle while the bright shell shows the lattice fringes with an interplanar spacing of 0.34 nm, which corresponds to the (0002) lattice plane of graphite.

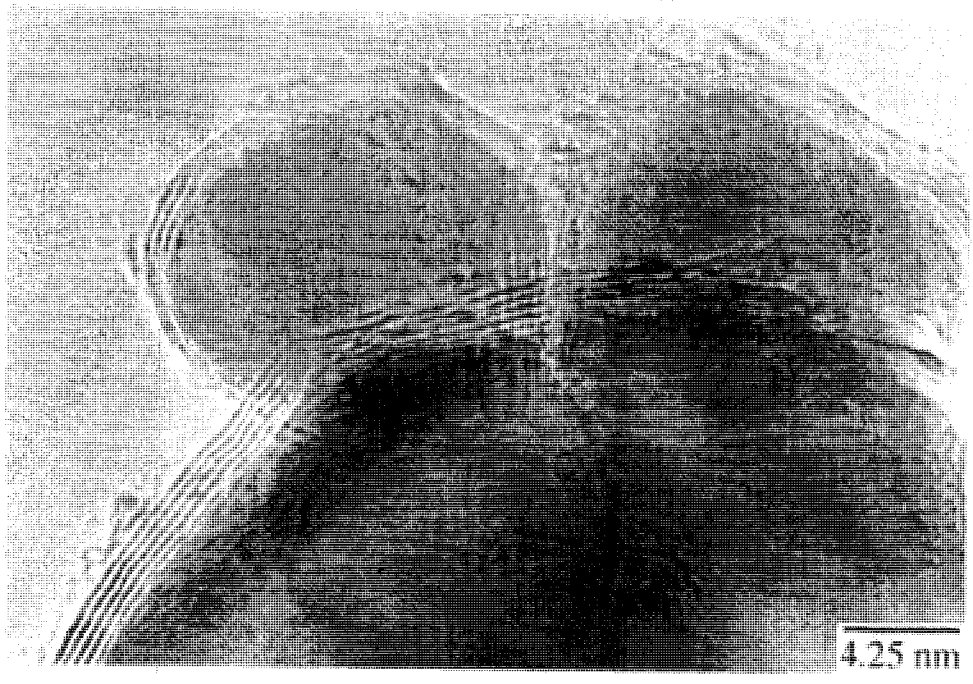

Figure 2.4 HRTEM images showing the shell–core structure of Fe(C) (Zhang, Z.D. et al., 2001)

Jiao *et al* did other modification to eliminate the formation of nanotubes or any other pure carbon composition (Jiao, J. et al., 1996). They used a graphite rod of 6.5 mm diameter as cathode and a graphite crucible with 25 mm inner diameter, filled with selected bulk material such as iron, cobalt or nickel, as anode. FE-SEM result (Figure 2.5) shows that no nanotube is produced and that the powder only consists of spherical particles.

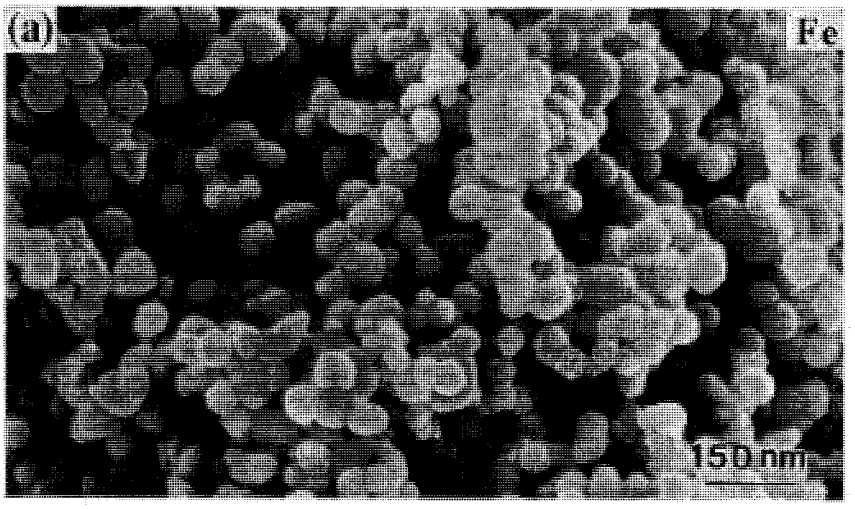

Figure 2.5 Encapsulated iron nanoparticles (Jiao, J. et al., 1996)

They also reported results of XRD, and showed that when iron is filled into the crucible the produced powder contains of γ-Fe (austenite) and α-Fe. They argued that the formation of austenite which is a metastable phase is due to rapid helium quench. They found no iron carbide in their produced powder.

2.6. Thermal plasma

2.6.1. The plasma state

Materials in plasma state exhibit special characteristics which make scientists consider them as a forth state of materials beside solids, liquids and gases. These special characteristics are due to the presence of considerable amount of free electrons and ions in the plasma. As an example, free ions and electrons increase the electric conductivity of plasma to those of metals. Properties of plasma will be separately discussed in subsequent pages.

Plasma produced by electric discharges can be divided in two categories; "thermal" or "equilibrium" plasma and "cold" or "nonequilibrium" plasma.

In a thermal plasma the temperature of electrons is equal to that of ions, atoms and molecules (heavy particles), therefore; there is a local thermodynamic equilibrium in the gas. This equilibrium is called local because of the high temperature gradient in plasma which causes local deviation from complete equilibrium. Thermal plasma is used because of its high

energy density mostly in material processing like particle synthesis, spheroidization, densification or protective layer deposition.

Cold plasmas are used for etching and deposition processes and in plasma surface modifications (Boulos, M.I., 1991). They are known for their low energy density and by the large difference between the temperature of electrons and heavy particles.

The difference in density and electron energy level of thermal and cold plasma is shown in Figure 2.6 (Boulos, M.I., 1991).

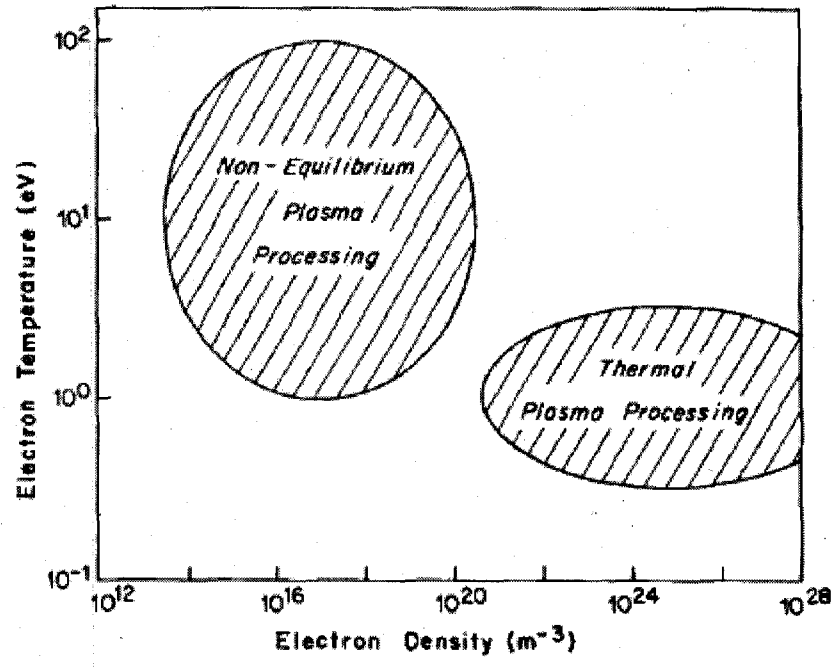

Figure 2.6 Typical range of electron temperature and electron density for thermal and cold plasma (Boulos, M.I., 1991)

2.6.2. Thermodynamic and transport properties

As it is mentioned in the previous part, presence of electrons and ions gives special characteristics to the plasma. In this part, properties of thermal plasma are briefly discussed.

The density of the free electrons and ions in the plasma depends on the temperature and on the gas properties such as its ionization energy and its nature. There are substantial differences between the thermodynamic properties of monatomic and diatomic gases.

Argon is the gas used mostly as plasma gas because it is monatomic and it has a low ionization energy. Due to these properties it is used for plasma generation because it ionizes better than other gases. A diagram of its composition versus temperature is depicted in Figure 2.7. In this diagram plasma is assumed to be in thermodynamic equilibrium.

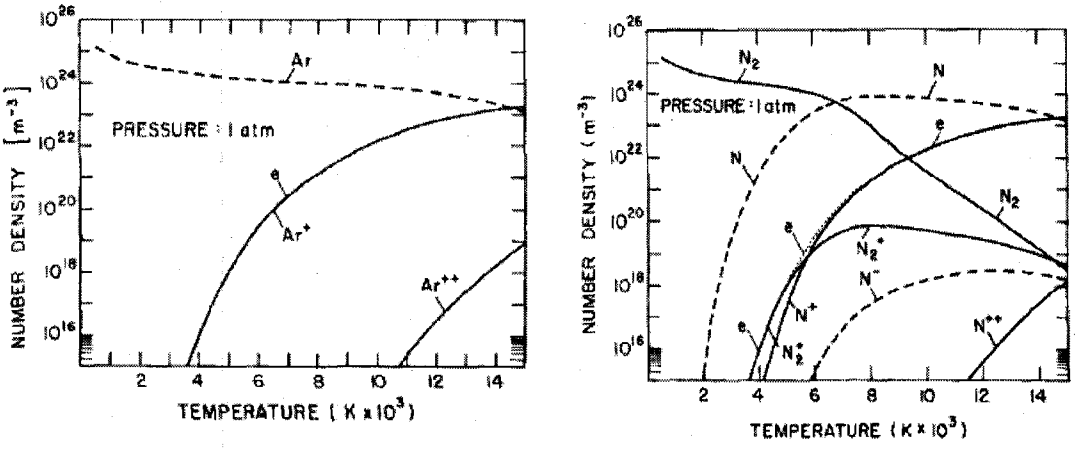

(a) (b)

Figure 2.7 Composition of (a) argon, (b) nitrogen, plasma as a function of temperature (Boulos, M.I., 1991)

Diatomic gases have a more complex composition in plasma state because first they can be ionized to form charged molecules or dissociated to its atoms. The produced atoms can also be ionized at higher temperature. In Figure 2.7 (b) the enthalpy behavior of nitrogen at high temperatures is shown. If we mix a monatomic gas with a diatomic one, we can benefit from advantages of each one.

The advantage of a diatomic gas is its high specific enthalpy as it is showed in Figure 2.8. By means of this property we can have a greater amount of energy per unit mass of diatomic gas at lower temperatures. This property is useful when a high amount of energy is needed and at the same time parts of the system should be kept away from extremely high temperatures. The specific enthalpy of some diatomic gases is presented in Figure 2.8 for comparison with that of monatomic gases.

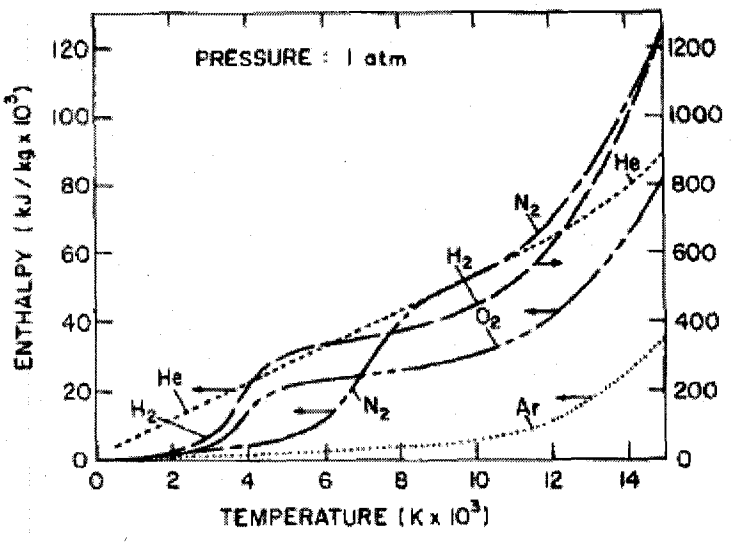

Figure 2.8 Specific enthalpy of some monatomic and molecular gases as a function of temperature (Boulos, M.I., 1991)

Another important property of gases for plasma processing is their thermal conductivity. Molecular gases near their dissociation temperature show a sudden increase in the thermal conductivity. This increase in thermal conductivity is due to the dissociation of molecules in hot region, which is an endothermic reaction, and then the combination of atoms to form the molecule in a cold region, which is an exothermic process. This mechanism transports huge amounts of energy from the hot zone to the cold zone and causes an increase in the thermal conductivity. Figure 2.9 shows the effect of hydrogen percentage in a H_2/Ar mixture on the thermal conductivity.

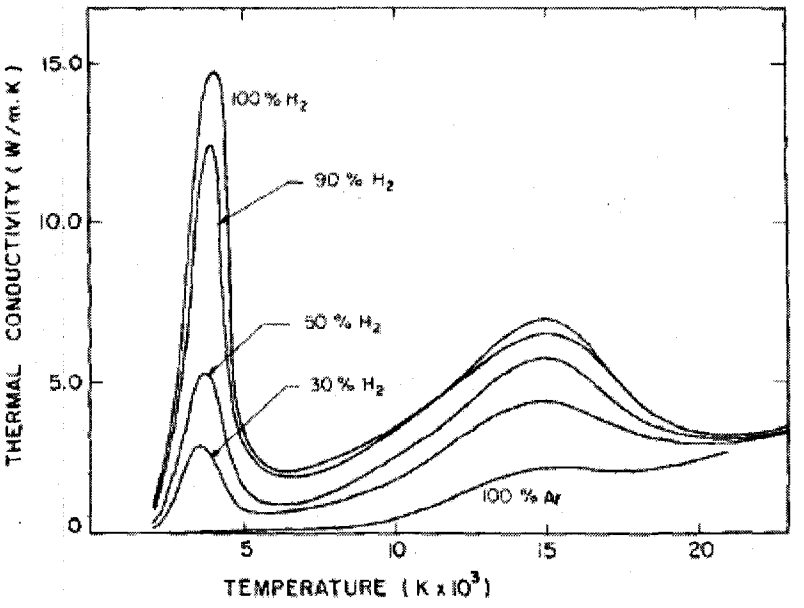

Figure 2.9 Thermal conductivity of H_2/Ar mixture as a function of temperature (Boulos, M.I., 1991)

As it is mentioned earlier in this chapter there is an important temperature gradient in the plasma reactor from the plasma "fireball" with temperatures around 10000K and the water-cooled reactor wall at a temperature around 350K which is 10-15 cm away from the plasma fireball. This temperature gradient influences the transfer properties of gases in the plasma reactor. Rahman *et al* calculated the transport properties of gases in the reactor using the computed temperature field in reactor (Rahmane, M. et al., 1995). The plasma gas was a mixture of argon and hydrogen (5% H_2 vol.) with a flow rate of 75 slpm. Nitrogen was injected as a cold gas into the middle of plasma gas to study mixture of cold gas with plasma gases. The power of the d.c plate was held constant at 20 kW. First, in Figure 2.10 the temperature, velocity and gas concentration profile is plotted as a function of the axial distance from the torch exit. Then in Figure 2.11 the transport properties of gases are presented in order to show the variation range of these properties in a plasma reactor. In Figure 2.10 dots show experimental data and the solid line represents modeling results. In Figure 2.11 contribution of laminar and turbulent mechanisms for each property is shown separately.

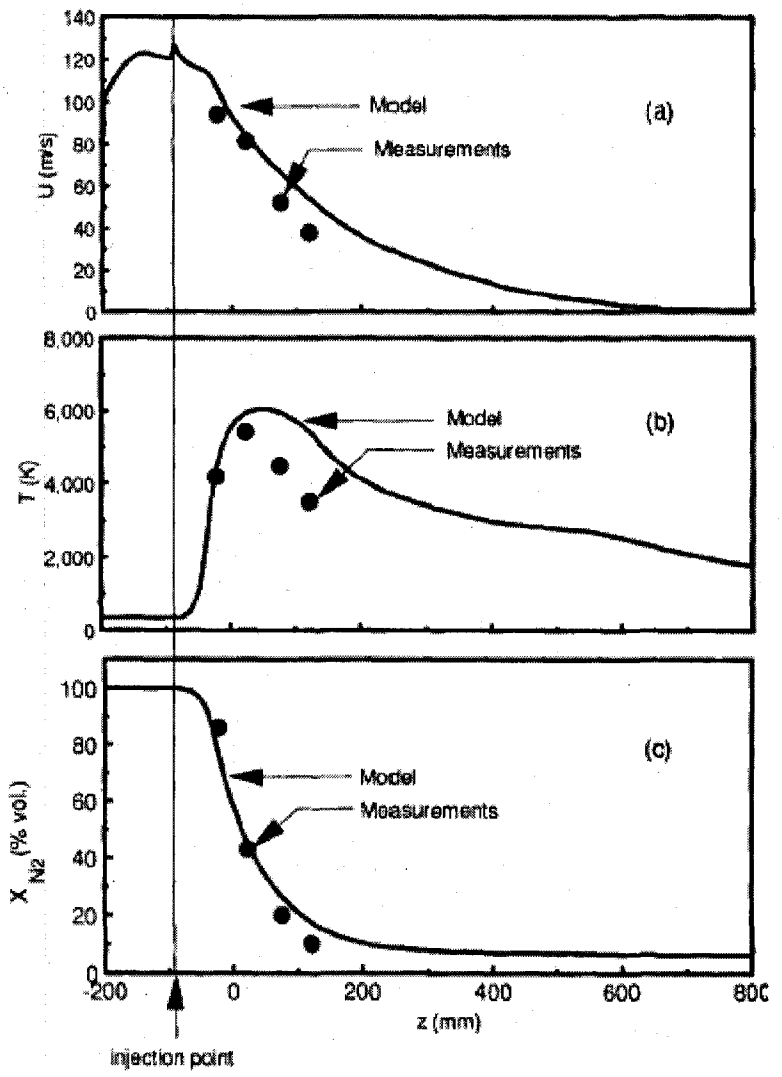

Figure 2.10 Axial profiles of the (a) velocity, (b) temperature and (c) injected gas concentration along the centerline of the torch-reactor system (Rahmane *et al* 1995).

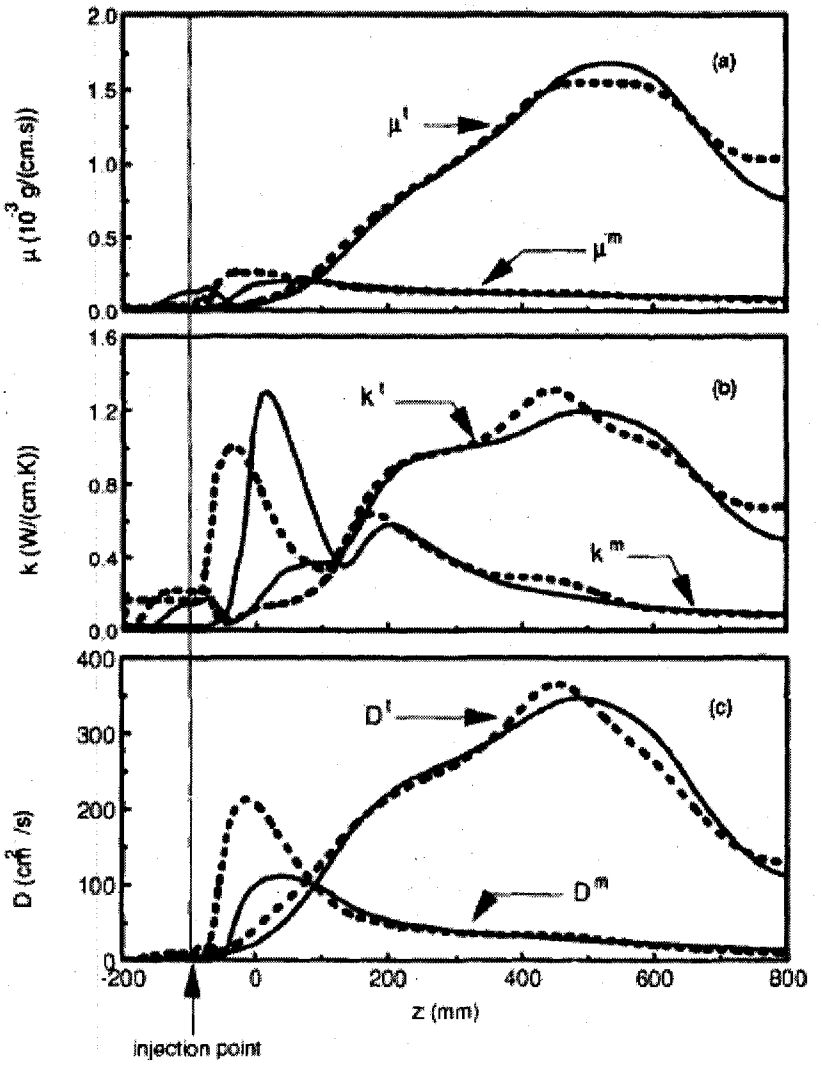

Figure 2.11 Axial profiles of the (a) viscosity, (b) thermal conductivity and (c) mass diffusivity along the centerline of the torch-reactor system.: (dot line) helium, (full line) nitrogen (Rahmane *et al* 1995)

2.6.3. Generation of radio frequency (RF) plasma

In RF plasma, an alternating electro magnetic field induces an eddy current in a process gas which is passing through the center of a water-cooled ceramic tube. The alternative electro magnetic field is generated by copper coils connected to a generator. The generator operates between 400KHz to 4MHz (Smith, R.W. et al., 1989a) and that is why it was called

"radio frequency plasma". Today, as radio frequency expanded, inductively thermal plasma is also widely used.

Several gas streams are introduced to the plasma torch. These streams include the powder gas Q_1, which is injected axially in the center of the plasma torch. This gas carries injected particles introduced by means of a water-cooled probe. The intermediate gas Q_2, is injected to the discharge zone and as the main gas for plasma stabilization. It has both axial and tangential velocity components (Boulos, M.I., 1991). The third and the outer one, is the sheath gas (Q_3). It serves to reduce the heat flux from the plasma gas to the confinement tube. The plasma torch dimensions and more details description of injected gases will be presented in chapter 3.

2.6.4. Nanoparticles synthesis by R.F plasma

RF plasma offers an attractive route for nanoparticles production. High temperatures and steep temperature gradients provide a great degree of supersaturation and it is the driving force for nanoparticles nucleation (Pfender, E., 1999). Nucleated particles quench rapidly in the reactor, and do not have enough time for further agglomeration. Another specific characteristic of thermal plasmas is its great energy density, which results in huge throughput in small reactor. In spite of these advantages, processing costs of this method compared to other methods is a major problem, and it must be offset by production of high value-added materials (Pfender, E., 1999).

Kameyama *et al* used a dual-R.F torch for production of iron carbide (Kameyama, T. et al., 1993b). The dual-R.F torch is composed of two electric coils. One coil is installed for primary ignition on the top and the other coil for reaction in the reaction chamber (Figure 2.12). The output of the first coil was 1.0 kW and that of the second one was 10 kW. They injected SiH_4-CH_4-$Fe(CO)_5$ as precursor.

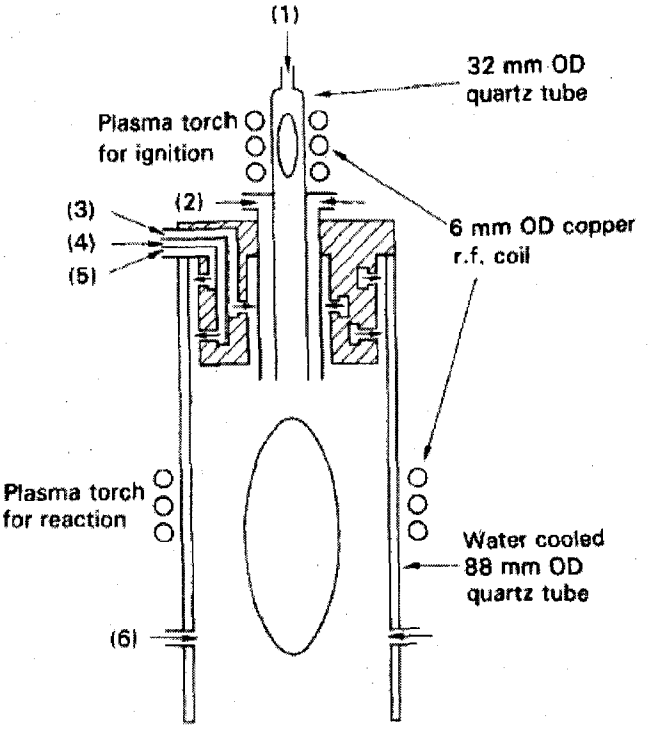

Figure 2.12 Schematic view of dual-RF torch (Kameyama, T. et al., 1993b)

Based on inductively coupled plasma spectroscopy they found that about 85% of the produced powder consists of iron-silicon alloy. The rest of the powder is a mixture of elemental silicon, iron, free carbon and silicon carbide.

TEM results of the produced powder shows that the powder contains conglomerates of small particles with diameters between 5 to 50 nm. Figure 2.13 shows particles collected from two different places of the reactor and they both show the same size distribution.

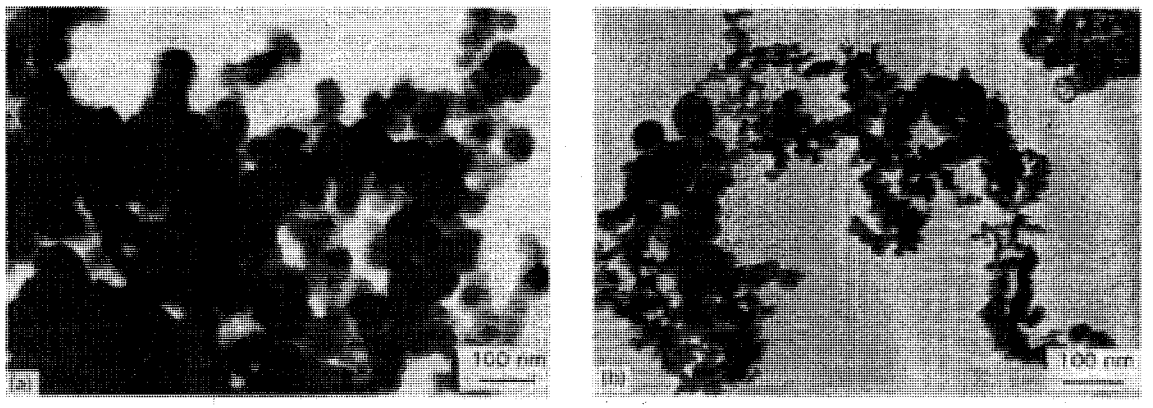

Figure 2.13 TEM images of Fe Si-C powder (Kameyama, T. et al., 1993b)

3. EXPERIMENTAL METHODS

In this chapter a description of the experimental methods used in this study will be described. In the first section, the experimental set up is presented. It will be followed by a description of the two (solid and suspension) injection techniques. Several characterization methods are used in this study and a brief description of each of them will be presented in section 3.4. For each characterization technique the operating parameters is also reported. The range of experimental parameters for nanoparticle synthesis is reported in section 3.5 and finally some theoretical backgrounds for factorial design and its interpretation is mentioned in section 3.6.

3.1. Experimental set up

In Figure 3.1 a schematic of the plasma torch, the synthesis chamber and the filters is represented. A PL-50 torch fabricated by Tekna is used in this set up as a device to convert electrical energy to heat. A copper coil in the torch is connected to a RF generator which operates at 3 MHz and a maximum plate power of 60 kW.

The PL-50 plasma torch consists of a 50 mm ID water-cooled ceramic tube. The copper coil surrounds the ceramic tube and conducts the electric current. On the top of the ceramic tube a gas distributor injects three gas streams. Central gas is injected tangentially into the middle of the ceramic tube. The central gas is ionized to form the plasma; hence, Argon is chosen because of its low ionization energy. The second gas injected into the torch is called sheath gas because it protects the ceramic tube from thermal shocks generated by the plasma. The sheath gas is injected along the ceramic tube and it consists of a mixture of argon and 13% of hydrogen. A quartz tube is placed between the central gas and the sheath gas to prevent the early mixing of two gases which could prevent plasma formation because of the high flow rate of sheath gas. The third gas injected into the plasma torch is the powder carrier gas. This gas carries powder precursor which will be injected by means of a water-cooled probe into the middle of the plasma region. A detailed schematic of the PL-50 torch and dimensions of this torch is represented in Figure 3.2.

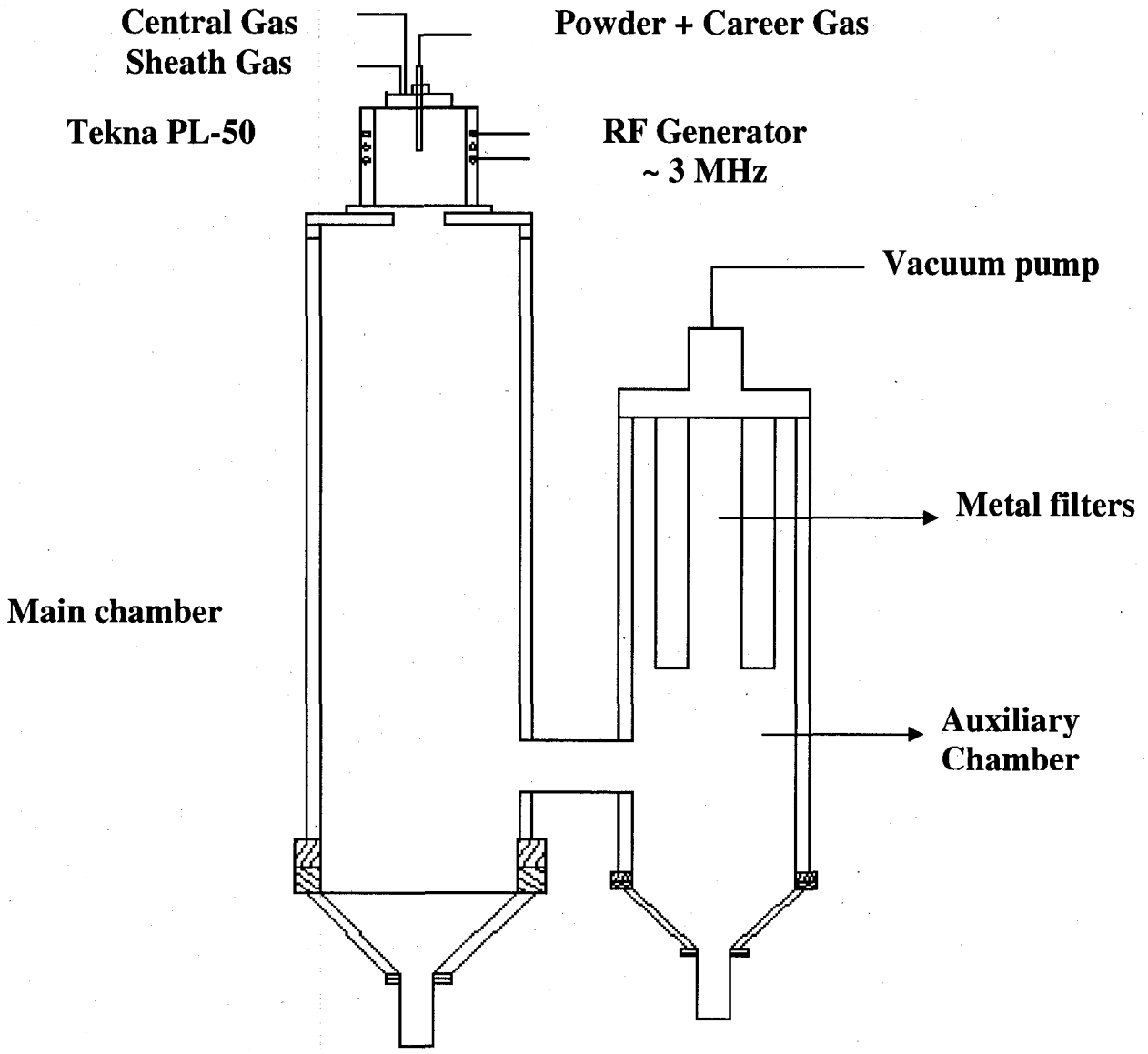

Figure 3.1 Experimental set up

$r_1 = 1.7$ [mm]
$r_2 = 3.7$ [mm]
$r_3 = 18.8$ [mm]
$R_0 = 25$ [mm]
$R_C = 33$ [mm]
$L_1 = 10$ [mm]
$L_2 = 74$ [mm]
$L_T = 250$ [mm]
$w = 2$ [mm]

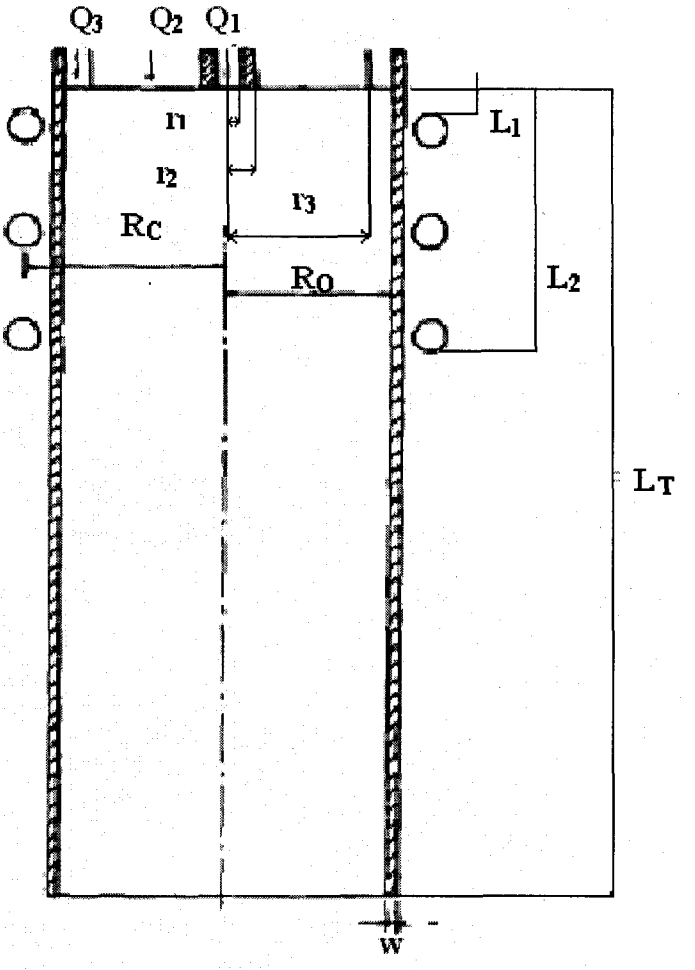

Figure 3.2 Plasma torch (Boulos, M.I., 1991)

Precursors are injected into the plasma region by means of an injection probe. Two different injection probes are used in this study, one for suspension precursor injection and the other one for solid precursor. These injection probes consist of a long water-cooled tube while in liquid injection probe a special design is used to atomize the injected suspension. In this probe another tube is located in the central part and liquid will be injected in the inner tube and the atomizing gas on the outer side. At the exit, the inner tube gas will atomize the liquid in the gas blast atomization nozzle (Figure 3.3).

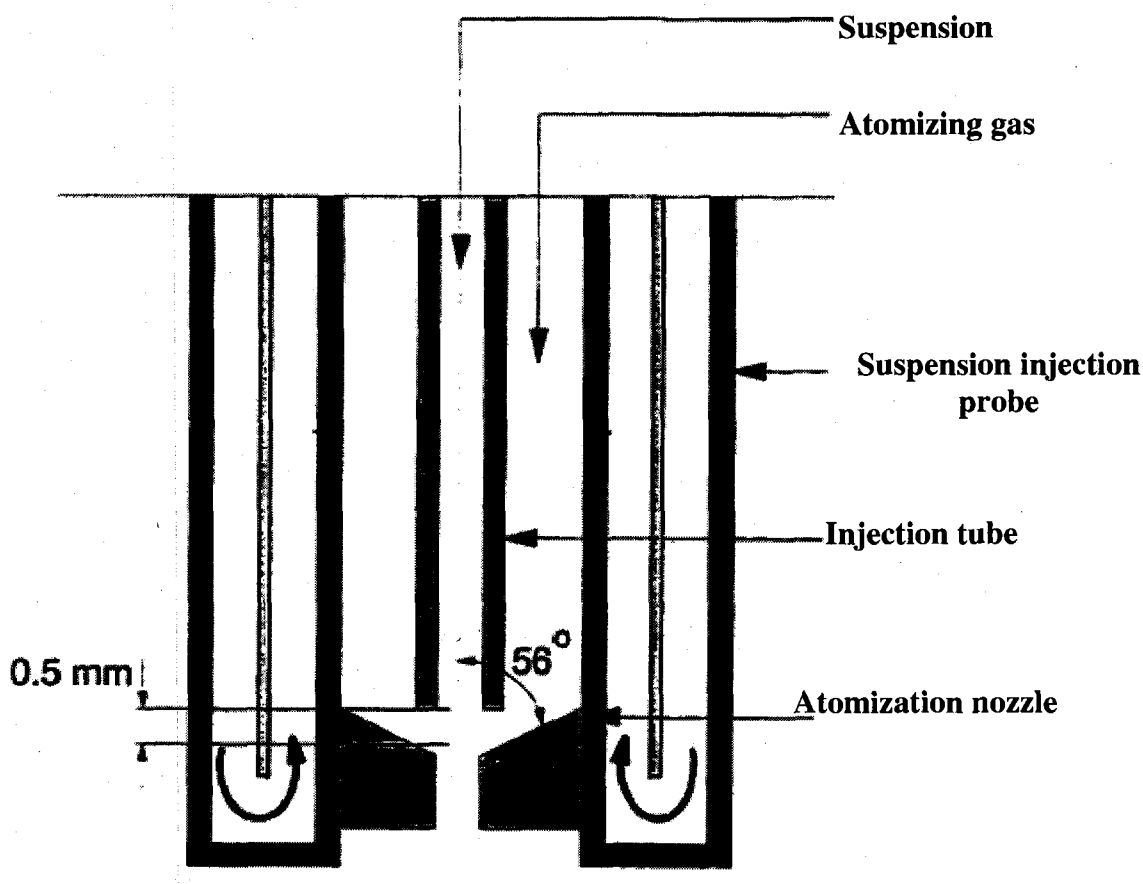

Figure 3.3 Suspension injection probe (Bouyer, E., 1997a)

Produced powder is deposited on the wall of main and auxiliary chambers and collected by four sintered metal filters. The main chamber is a water-cooled cylinder with 24 cm ID and 103 cm of length. The auxiliary chamber is also a water-cooled cylinder with 20 cm ID and 72 cm of length. The auxiliary chamber is connected to the vacuum line with a control valve in order to adjust the pressure in the main chamber.

3.2. Injection techniques

As mentioned in the previous section, two injection methods are used in this study. In both methods, spherical iron particles with diameter between 1 and 5 μm are used. In Figure 3.4 SEM images of these particles are shown. This iron powder is purchased from Alfa Aesar Company.

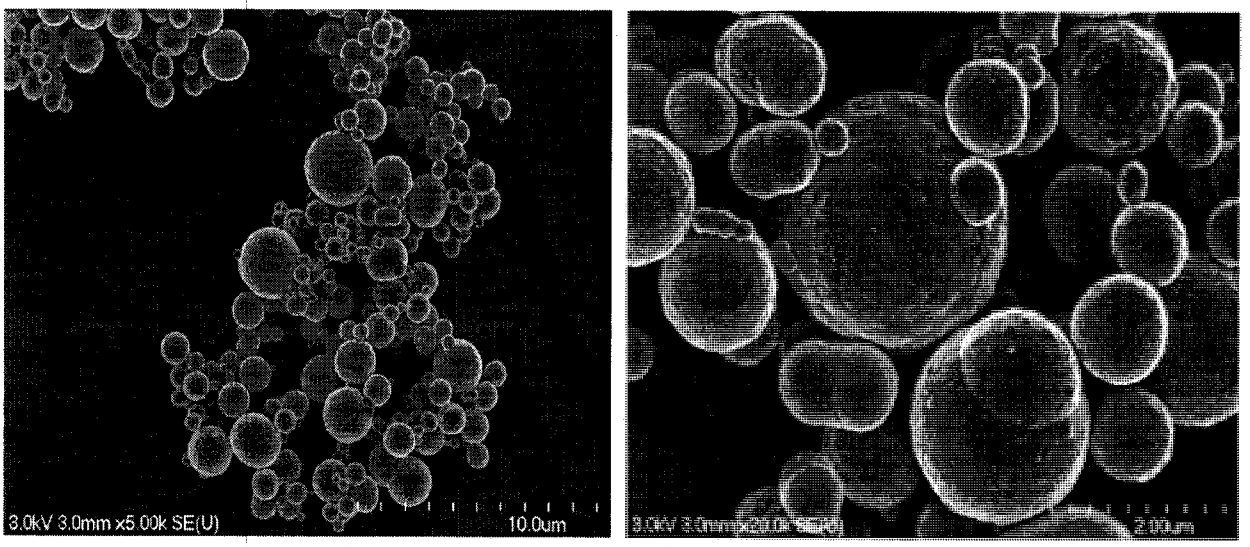

Figure 3.4 SEM images of initial iron particle

As It is shown in this picture, the initial iron particles have smooth surface and are aggregated in some cases. In solid injection method iron powder is injected by means of a positive displacement powder feeder (Sylco CCC Model Mark IX). With this powder feeder iron powder is loaded into the main chamber. The wall of the main chamber vibrates in order to prevent powder agglomeration and bridging during the injection. On the bottom of the main chamber a rotating screw conducts the powder from the main chamber to a cyclone. In the cyclone the iron powder is entrained by the career gas to the injection probe. The injection rate of the powder feeder depends on the rotation speed of the screw and also to the pitch of the screw. The advantage of this powder feeder its the positive displacement mechanism, the bridging effect will become less important during injection of micrometric and nanometric powders. The remaining powder can be removed from the main chamber by tilting the

instrument. Calibration and mass balance is done by subtracting the mass of remaining powder from the initial mass and divide the result by the total injection time.

In the suspension injection technology, the main objective is to produce a homogenized liquid with desired viscosity to prevent the blockage of the injection probe. A stirrer is used to disperse solid particles in the suspension and also an external recirculation circuit is added to remove the liquid from the bottom of the suspension container and to pump it to the top section. Bouyer *et al.* recommended 0.8 Pa.s as the maximum suspension viscosity for a continuous suspension injection without probe clogging (Bouyer, E. et al. 1997b). Several tests were conducted to find the ideal suspension composition and minimum liquid injection rate for a continuous injection without blockage. It was found that a mixture of 30 gr of iron and 150 ml of mineral oil (Fischer Scientific, CAS : 8042-47-5) is the ideal mixture and minimum liquid injection rate is 5 ml/min. The viscosity of the suspension was not measured by a viscometer in this study but it is recommended to do it, since the viscosity of the suspension affect the diameter of sprayed droplet produced by the atomizer based on Lefebvre equation (Bouyer, E. et al 1997b). The suspension with above composition forms a homogeneous liquid and this assumption can be verified by measuring the amount of solid in remained liquid at the end of experiment. If the solid to liquid ratio at the remaining liquid is equal to the initial ratio, it can be concluded that solids are not accumulated on the bottom of the container and the mixing and the recirculation have provided a good dispersion of solid in the liquid. In order to pump the suspension from the container to the injection probe, a Masterfelx pump (HV-77340-00) is used. The minimum injection rate for this pump is 3 ml/min for L/S 13 tube. The same model pump is used for circulation with a L/S 16 tube and 2000 ml/min flow rate for a high flowrate suspension circulation. The low injection velocity may cause solid sedimentation through the connection tubes and the suspension entering the atomized may not be homogeneous. The weight difference between the connection line before and after each experiment is measured and it did not show any significant difference and it shows that no solid sedimentation has occurred during the injection. However, this overall calculation can not guarantee that each atomized droplet at the atomization probe exit is homogeneous.

3.3. Wet collection method

During the synthesis of nanoparticles in plasma system, the produced particles are deposited on the main chamber wall, the auxiliary chamber wall or they are captured by sintered metal filters installed in the auxiliary chamber (Figure 3.5). In order to recover these powders, the main chamber is separated from the plasma torch, system is dismantled and then the wall of the reactors is brushed to collect the produced powders.

This procedure has two disadvantages. First, some of the produced nanometric particles are pyrophoric and react immediately with oxygen. This collection method exposed particles to the air during the collection procedure. Secondly, they are dispersed into the air during the brushing and could be inhaled by laboratory staff and students.

A device is designed to collect the produced powder with an inert liquid. This prevented particles exposure to oxygen and their dispersion into the air.

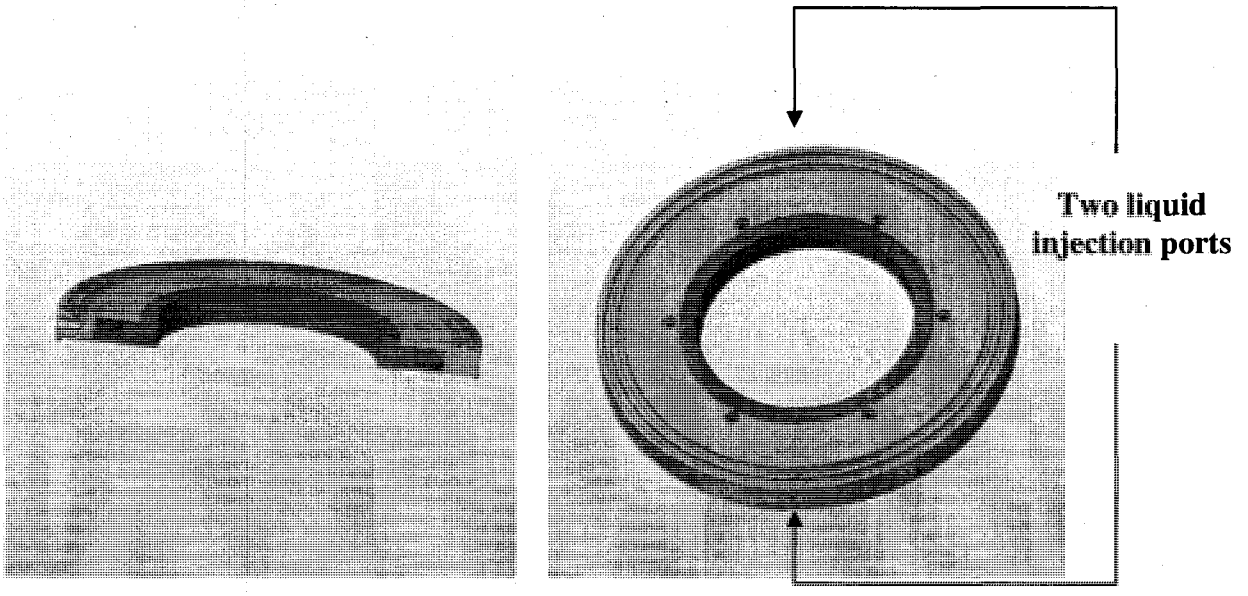

Figure 3.5 Two schematic view of liquid injection flange

Figure 3.5 shows a schematic view of the designed flange. This flange consists of two separate parts. When these parts are connected together a narrow channel is formed for liquid circulation. There is a slit on the bottom of this channel where the liquid leaks through and

enters the collection chamber. This flange is installed on the top of the main chamber and the leaking liquid forms a thin liquid film and wets the wall of the chamber. Figure 3.6 shows the liquid film formed for wet collection method.

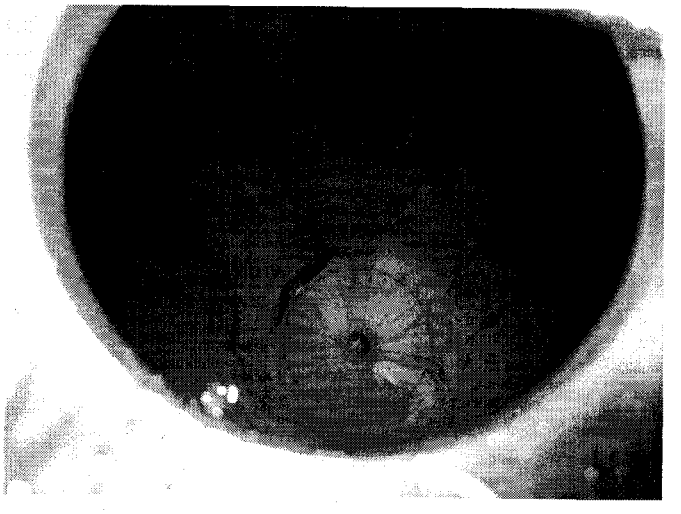

Figure 3.6 Liquid film formation during wet collection

Up to 90% of the produced powder are collected by this method and separated from the liquid by centrifugation. The collecting liquid must be compatible with produced powder. In our study decalin (Decahydronaphthalene) for wet collection is used because it will be used as the liquid medium in slurry phase FTS reactor. This method has a great advantage for nanoparticle storage and transportation.

The results reported in the next section are obtained by dry collection method to minimize any possible effect of liquid on the produced powder and also to eliminate powder drying which could influence the morphology and chemical composition of the produced powder.

3.4. Characterization techniques

In Table 3.1 a list of characterization methods used in this study is presented. These methods are used in order to determine the morphology, size and chemical composition of the produced particles.

Table 3.1 List of characterization methods and their applications

Physical or chemical properties	Method used
Morphology and size of particles	▪ Scanning electron microscopy (SEM) ▪ Transmission Electron Microscopy (TEM) ▪ High Resolution Electron Microscopy (HRTEM)
Qualitative phase composition	▪ High Resolution Electron Microscopy (HRTEM) ▪ X-ray Diffraction (XRD)
Qualitative phase composition	▪ X-ray Diffraction (XRD) ▪ Thermogravimetric analysis (TGA)
Crystallite size	X-ray Diffraction (XRD)
specific surface area	BET analysis

Several techniques are used to determine the morphology and size of particles because preliminary results revealed that the powder consists of a broad range of particle size; hence, we used SEM was used for particles greater than 1 micron and TEM and HRTEM for nanometric particles. XRD was used to identify the bulk composition of powder and HRTEM was used to verify the phase of individual particles. TGA was used to measure the total amount of carbon in the produced powder.

X-ray Diffraction

In XRD, a Cu anticathode is bombarded by a beam of electrons. Copper atoms are exited as the result of electron bombardment and when they return to their fundamental state, they emit photons (X-rays). This beam will be collimated to illuminate the powder sample.

In this method the sample preparation consists of hand pressing of 1 to 2 grams of powder into a square shaped sample holder. No grinding before analyse is made because there is no preferential direction in nanometric powders.

X-ray source and X-ray detector are rotated around the sample in order to change the angle between the X-ray beam and the sample. According to Bragg's law (Equation 3.1), in a certain angle, the X-ray will be diffracted after diffraction from the sample. A detector measures the intensity of diffracted beam and intensity and corresponding angle is sent to a computer.

Bragg's law is represented by the following equation:

$$n\lambda = 2d \cdot \sin\theta \qquad (3.1)$$

Where:

- n is an integer determined by the order given
- λ is the wavelength of x-rays
- d is the spacing between the planes in the atomic lattice
- θ is the angle between the incident ray and the scattering planes

By comparing the angles of the intense peaks with the standard data from JCPDS (Joint Committee on Powder Diffraction Standards) files, the existing phases are identified. JADE 6.0 software uses the absolute intensity of several peaks to perform a semi-quantitative analyse.

Transmission Electron Microscopy

In a TEM, a beam of electrons originate from an electron source and is focused and confined as it passes through electromagnetic lenses and apertures. Thermionic and field emission guns are two kinds of electron sources used in TEM. In a thermionic gun, a filament (LaB_6) is heated until it emits a beam of electron with the desired brightness. In a field emission gun, the electron beam is created by an electrostatic field.

Once collimated, the electron beam reaches the sample. A part of the beam interacts with the sample and deviates or diffracts by the atoms of the sample while the other part is

transmitted through the sample. Another set of electromagnetic lens focuses these different beams and an image of the sample appears on a fluorescent screen or is recorded on a CCD camera.

In this study, a Hitachi H-7500 is used for low resolution TEM imaging and a JEOL JEM 2010F is used for high resolution images. In high resolution images, the lattice d-spacing of particles is observed and compared to other results to determine the composition of well crystallized particles.

Scanning Electron Microscopy

Typically, the same source of electron is used in SEM or TEM. The main difference in SEM is the mechanism of image formation. Once the electron beam, strikes the surface of the specimen, the exited atoms in the specimen return to their stable state. The excess energy of the incident electron is mainly released as secondary electrons or backscattered electrons. The excited atoms return to their fundamental state by emission of characteristic X-Ray or Auger electrons. The intensity of the electrons is used to produce an image of the specimen.

Two types of detectors are used the SEM. Backscattered electron detector is used to detect a fraction of the electron beam which leaves the sample surface after a number of elastic collisions. The number of backscattered electrons depends on the atomic number of the bombarded element, hence; atoms with higher atomic number produce more backscattered electrons and they produce brighter images. Secondary electron detector is another type of detector. Secondary electrons are produced as a result of inelastic collision. After these collisions, the bombarded atom liberates an electron from the outer quantum level to return to its stable state. These electrons have a much lower energy (around 50 eV) than backscattered electrons and they will be attracted by a biased grid placed (200 V) on the secondary electron detector. This grid cannot attract backscattered electrons because they have a too high energy.

In this study a field emission SEM is employed to see the size of the particles and their morphology. The Hitachi H-4700 SEM is used with a 3kV accelerating voltage to take pictures with magnifications up to 150k.

Thermogravimetric Analysis

In TGA analysis, two or three mg of the sample is loaded into the sample holder and placed into an isolated chamber in which 50 ml/min of air is injected. The temperature ramp

rate is set at 10°C/min and it increases from 50 to 960° C. The weight of sample is measured and a diagram of the weight change versus temperature is obtained.

For the synthesized iron carbide particles, carbon atoms will react with oxygen and leave the sample by forming CO or CO_2 molecules. During the heating process iron atoms will also transform to iron oxide. It is assumed that when there is no change in weight, all carbon atoms have already left the sample and all iron atoms will have been oxidized completely.

3.5. Operating conditions

In this study two sets of experiments were conducted to investigate the formation of nanosize iron carbide particles. First, preliminary tests were performed in order to find suitable carbon donor precursor. In these tests, 2-butanol was the main source of carbon atoms and glycerol was used to increase the viscosity of the suspension and to increase the settling time of iron particles in suspension. In Table 3.2 the range of parameters used in this study is listed.

Table 3.2 Preliminary tests experimental conditions

Parameters	Condition
Precursor	25 g Fe 25ml Glycerol 50ml Butanol
Plate Power	25-45 kW
Reactor Absolute Pressure	300 Torr
Injection Probe Position*	65 mm
Injection flow rate	10 ml/min
Gas flow rate: Central Sheath Career	 Ar:23 L/min (STP) Ar:75 L/min (STP) H_2 10 L/min (STP) Ar:11 L/min (STP)

* Measured from the exit of the plasma torch

Once the preliminary tests were completed, a 2^n factorial design was used to identify the preferential operational conditions. More details of the experimental runs are given in the next section. In Table 3.3, plasma parameters ranges in this section are listed.

Table 3.3 Experimental parameters for factorial design runs

Parameters	Condition
Precursor	60 g Fe 300 ml mineral oil
Plate Power	25-55 kW
Reactor Absolute Pressure	300 Torr
Injection Probe position	65-75 mm
Injection flow rate	5-10 ml/min
Gas flow rate	Idem Table 3.2

The effect of injection of gaseous carbon donor precursor is also investigated in the third part of this thesis. Experimental parameters used in this section are presented in Table 3.4.

Table 3.4 Solid injection experimental conditions

Parameters	Condition
Precursor	Fe: 3-4.5 g/min C_2H_2: 0.3-6 L/min (STP)
Plate Power	45 kW
Reactor Absolute Pressure	300 Torr
Injection Probe position	65 mm
Gas flow rate:	Idem table 3.2

3.6. Experimental design

In this study, a 2^k factorial design was used to investigate the effect of plasma processing parameters on the conversion of iron to iron carbide. 2^k factorial design is mostly used to investigate the interaction effect of the factors in response.

2^k factorial design is a useful method in early stages of experiments, when many factors may influence the final results (Montgomery, D., 2001). There is also mentioned that this design is widely used in factor screening experiments.

Plate power, injection probe position and injection rate are three factors selected for a factorial design because of their possible influence on plasma temperature and residence time of particles in the plasma zone.

One of the main criteria to consider in factorial design is the increase of the distance between low and high level of design factors. Low level and high level of each factor is determined considering the operational range of plasma torch and plasma stability (Table 3.5). More detail of levels determination is given in the next chapter.

Table 3.5 2^3 statistical factorial design

Parameter	Coded factor	Low level	High level
Plate power kW	A	25	55
Injection flow rate (ml/min)	B	5	10
Probe position	C	6.5	7.5

Statistical analysis is done using Design Expert software 6.0.1 version developed by Estate Ease Inc. This software produces the ANOVA table and performs other calculations related to factorial design. Obtained results are presented and interpreted in chapter 4.

4. RESULTS AND DISCUSSIONS

4.1. Overview and objectives

Production of nanometric iron carbide particle is the goal of this project. Several factors like nature of the precursor, injection flow rate, plate power and probe position are among the main factors which may influence the conversion extent and the size of the produced particles.

The objective of this section is to investigate the effect of process parameters on conversion and size distribution of the produced particles. The effect of injected precursor nature by using suspension and solid injection techniques are also determined. Each of these methods has its own advantages and disadvantages and may produce different results.

4.2. Suspension Injection: Preliminary results

4.2.1. Objectives

The objectives of this section are to find out the feasibility of iron carbide synthesis in the plasma reactor. Thermodynamic analysis is used to investigate iron carbide formation at high temperatures and some predictions are made based on these results. Preliminary tests are also done to verify these predictions in practice. The possible operational conditions and solve the technical problems which may happen during the experiments are the main target of this work.

4.2.2. Thermodynamic analysis

Thermodynamical analysis can help predict the formation of different phases at the plasma reactor conditions. As it is shown in Figure 2.10, temperature changes extensively in the reactor; hence, the injected particles are exposed to different temperature zones. It is assumed that the system will reach equilibrium very fast at high temperatures, hence the thermodynamic equilibrium state of the system can be used to predict the final product in the reactor. To consider this assumption, it is supposed that the quench will stabilize the high temperature formed phases as room temperature metastable phases.

Zhao *et al* compared two different modeling results in their article (Zhao, G.Y. et al., 1990). In the first modeling result, the authors assumed that species are in chemical

equilibrium in the plasma reactor; in the second one they used kinetic data and calculated concentration of species by mathematical modeling. They found that in a high temperature zone, which is the case in most part of the plasma reactor, there is no substantial difference between the two results. In another article, Chang *et al*, tried to predict the final product composition in a plasma reactor by using thermodynamic analysis of the system (Chang, Y. et al., 1987). In their work, they used the Gibbs energy minimization to calculate concentration of each of the chemicals in equilibrium state. When they compared their results with experimental data they found that once a solid phase is formed in high temperatures, no further transformation to other molecules in lower temperatures were noted.

Based on these two works we the FactSage 5.5 software was used to illustrate a thermodynamic diagram to predict the feasibility of iron carbide production. The software is based on the Gibbs energy minimization to calculate equilibrium concentration of each of the materials.

In Figure 4.1, thermodynamic equilibrium curves of the system in term of the temperature is shown with butanol, glycerol and iron as precursors. The reason for choosing these materials will be discussed in section 4.2.3.

0.017 Fe + 0.02 $C_3H_8O_3$ + 0.36 $C_4H_{10}O$ +4.4 Ar +0.4 H_2

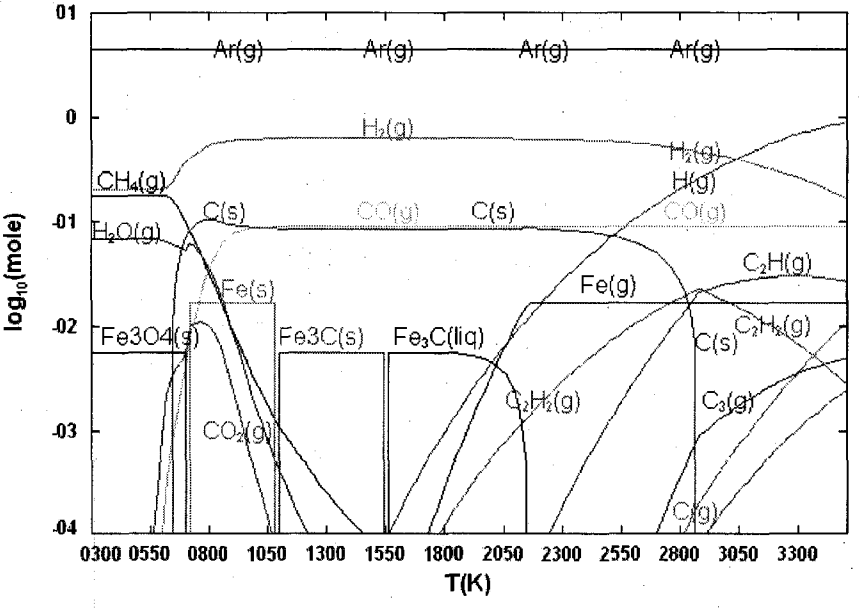

Figure 4.1 Thermodynamic equilibrium of the butanol/glycerol/iron system

Results of this diagram show that, all of the oxygen in the system reacts with carbon atoms to form CO at high temperatures. Liquid iron carbide is formed at 2000 K and it solidifies at 1600 K. Thermodynamic analysis shows that iron oxide produced at 750 K from pure iron. The validity of results obtained by thermodynamic analysis will be examined by running preliminary tests.

Figure 4.2 shows the thermodynamic behaviour of the system when mineral oil is injected with iron particles as precursors. Since oxygen was excluded from the system, no iron oxide was formed. In this figure solid carbon will be formed at 3000 K and liquid iron carbide at 2300 K which then transforms to solid iron carbide at about 1600 K.

0.01 Fe + 0.017 $C_{10}H_8$ + 4.4 Ar + 0.4 H_2

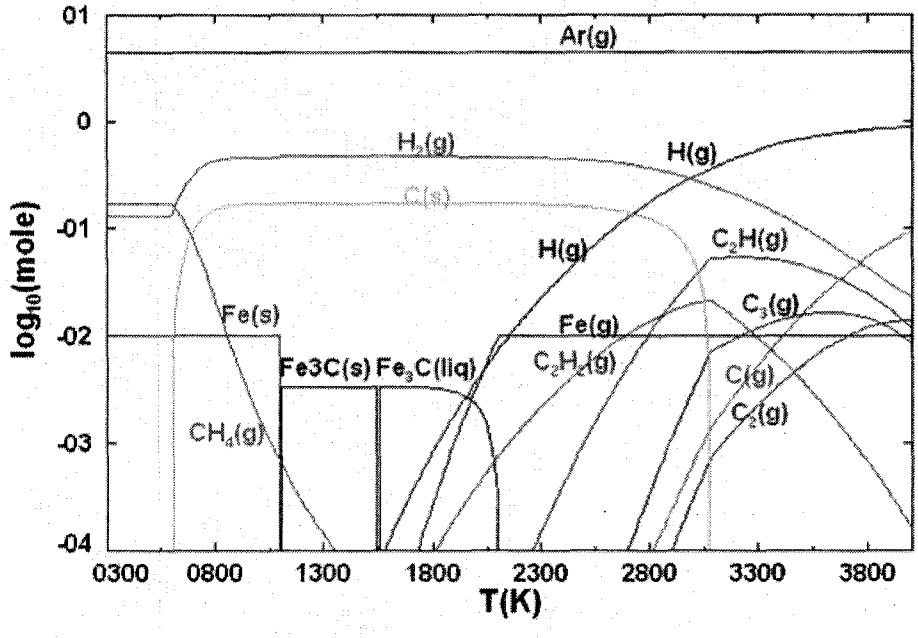

Figure 4.2 Thermodynamic equilibrium of mineral oil/iron the system

Results of Chang *et al* described above, show that once iron carbide is formed, it may not decompose to pure iron at lower temperatures. Only reactions with high kinetic rate may proceed significantly at low temperatures. It may be concluded from thermodynamic analysis that most of the carbon will be condensed as free carbon and that iron carbide will be

produced as the result of elemental iron reacting with carbon containing radicals or molecules. At low temperatures; chemical equilibrium may not be a valid assumption, based on the work of Zhao *et al* (Zhao, G.Y. et al., 1990)

4.2.3. Preparation

Preparing a homogeneous suspension was one of the steps in suspension injection method. Even in the presence of a mechanical stirrer some stagnation points may occur in the container. These stagnation points normally form on the bottom of container beneath the stirrer axis.

When liquid level decreases below the stirrer tip, smaller portion of stirrer mechanical energy will be transferred to the liquid, hence; solid sedimentation can take place. In order to increase the homogeneity of the suspension the sedimentation velocity of particles in the liquid must be decreased.

Sedimentation velocity of particles in a liquid can be determined using Stokes' law for Reynolds number less than 0.1 (equ. 4.1).

$$w = \frac{2(\rho_P - \rho_F) g r^2}{9\mu} \qquad (4.1)$$

Where:

- w : settling velocity (m/s)
- ρ : density (the subscripts p and f indicate particle and fluid, respectively), (kg/m^3)
- g : acceleration due to gravity, (m/s^2)
- r : radius of the particle (m)
- μ : dynamic viscosity of the fluid. (Pa.s)

Butanol, the liquid chosen as precursor was mixed with 33% vol. of glycerol to increase the viscosity of the suspension. Another candidate precursor for liquid was mineral oil. Based on vendor information purchased mineral oil is a mixture of heavy paraffins. Investigation of the effect of oxygen by using these two precursors was made.

As it is shown in Stokes' equation, by increasing the viscosity of the liquid the sedimentation velocity of the particles in the suspension is decreased. In the case of mineral

oil with a kinematic viscosity of 33.5 cst and for iron particles of 1 μm in diameter sedimentation velocity is $3.47*10^{-6}$ m/s. However, formation of iron particle aggregates (Figure 3.4) increases the sedimentation velocity. When this velocity is used to calculate the Reynolds number, a value of $0.7*10^{-6}$ is obtained which shows that Stokes' law is valid. In this calculation an average particle diameter of 1 micrometer is assumed.

Several trial and error tests were performed to find the appropriate concentration of iron particles in the liquid medium. These test were performed with the injection system separated from the plasma torch. The injection system is comprised of three parts: suspension recipient, peristaltic pump and injection probe. Solid concentration above 0.33 g/ml will cause probe clogging. Minimum injection rate was also found to be 5 ml/min.

In all powder production experiments, unknown amounts of oxygen entered into the reactor. Several ways were tried to minimize this amount but it was not possible to eliminate it completely. There was concern about possible effect of oxygen in the system so a protocol was developed to keep this amount constant for all experiments.

To examine the amount of oxygen entering into the reactor the pressure of the reactor was reduced to 300 Torr by means of a vacuum pump. The reactor was then disconnected from the vacuum line until the pressure of the reactor reached 350 Torr. This pressure increase is due to air entering the reactor from leakages. All suspected points of leakage were examined until the required time for this pressure increase reached 90 to 120 seconds. This protocol is used for all experiments in order to control experimental error under an acceptable level.

4.2.4. Oxygen containing precursors

In these series of tests a mixture of 2-butanol and glycerol is used as the liquid precursor in suspension. Experimental condition of these tests is presented in Table 4.1. In this study the pressure is held constant at 300 Torr during these tests and further in this study. Central Ar gas is set at 23 L/min (STP) while sheath gas is a mixture of Ar at 75 L/min (STP)) and H_2 at 11 L/min (STP) unless specified otherwise.

Table 4.1 Experimental condition, oxygenate precursor

Test Number	Atomizing gas L/min (STP)	Precursor			Plate Power kW	Injection rate ml/min
		Fe	$C_4H_{10}O$	$C_3H_6O_3$		
OL-1	Ar: 10	25 g	50 ml	25 ml	25	10
OL-2	Ar: 10	25 g	50 ml	25 ml	35	10
OL-3	Ar: 10	25 g	50 ml	25 ml	45	10

XRD results of tests OL-1 and OL-2 were almost the same (Figure 4.3).

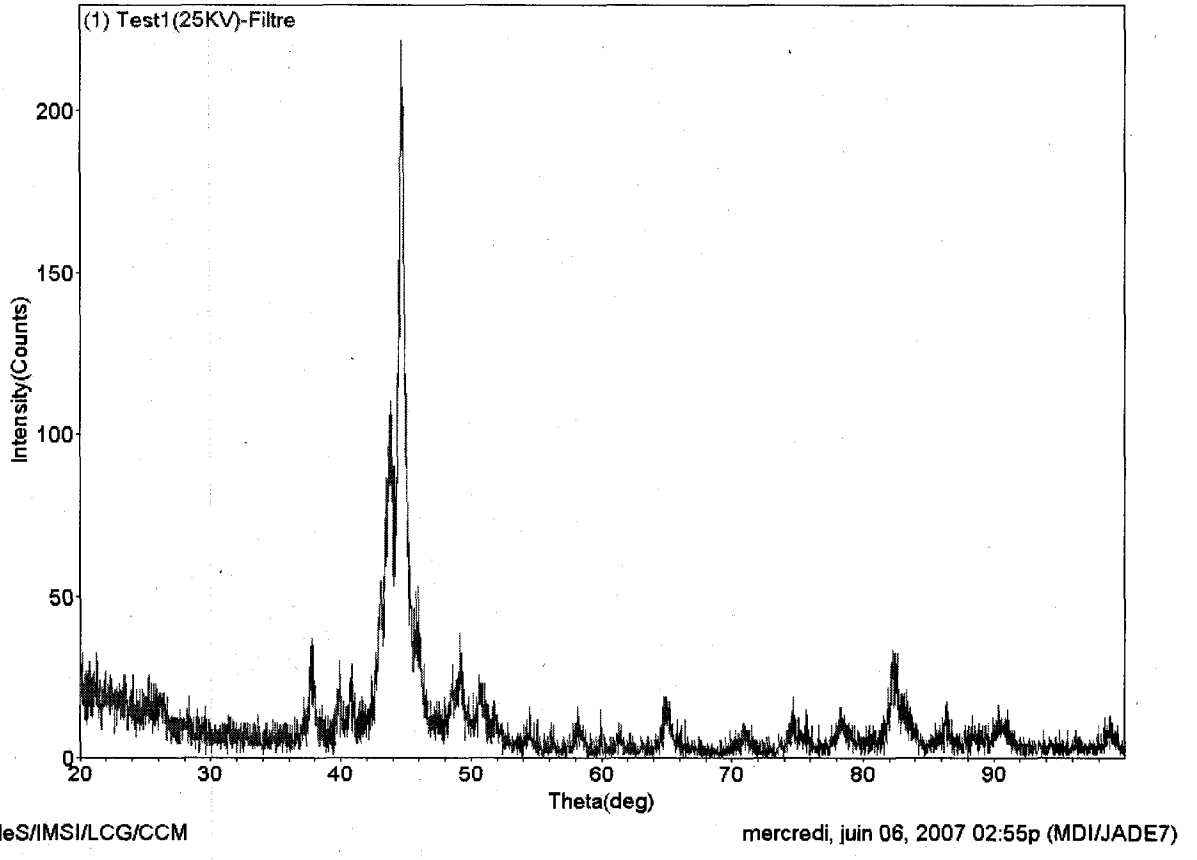

Figure 4.3 XRD result of OL-1

In Figure 4.3 the intense peaks at 2θ values of 44°, 65° and 85° match with pure iron peaks (JCPDS 087-0721) and peaks at 43° and 50° indicate the presence of austenite in the powder (JCPDS 052-0512). Single peak at 2θ = 37 and double peaks at 39-40 and 48-49 and also all less intense peaks between 50 and 60 match very well with the standard cohenite file (JCPDS 089-2722). The only peak representing the formation of graphite in the obtained powder is at 2θ = 26°. This peak corresponds to graphite's most intense peak (100%) representing (002) plane (JCPDS 075-1621).

In summary, four phases are formed by this method. Formation of austenite is due to rapid quenching of the gases. Intense temperature gradient in the RF plasma causes the formation of this unstable phase. The formation of unstable austenite is also reported in other researchers' works (Jiao, J. et al., 1996). Cohenite is the most stable iron carbide in iron-carbon phase diagram (Farhat, S. et al., 2006). Peaks of other iron carbide phases (Fe_7C_3, Fe_5C_2, and Fe_2C) were not detected by XRD method, but their presence cannot be ruled out completely at this stage. Formation of a graphite layer on the surface of iron carbide particles is also reported in the literature as was described in chapter 2. The graphite peak at 26° is broad and it shows that it has a low crystallinity.

SEM images of test OL-1 shows formation of two ranges of particle sizes. Figure 4.4 (a) is taken using secondary electron detector and shows nanometric particles. The nature of these particles is not known at this stage. Figure 4.4 (b) is taken using the backscattered electron detector. The number of backscattered electrons leaving the surface of the specimen depends on the atomic number of the targeted atom. In this case atomic numbers of iron and carbon are so different that areas with high density of iron atoms are brighter than the other areas. In this picture we can see bright spherical particles with diameter between 1-5 μm which have similar morphology to the injected iron particles.

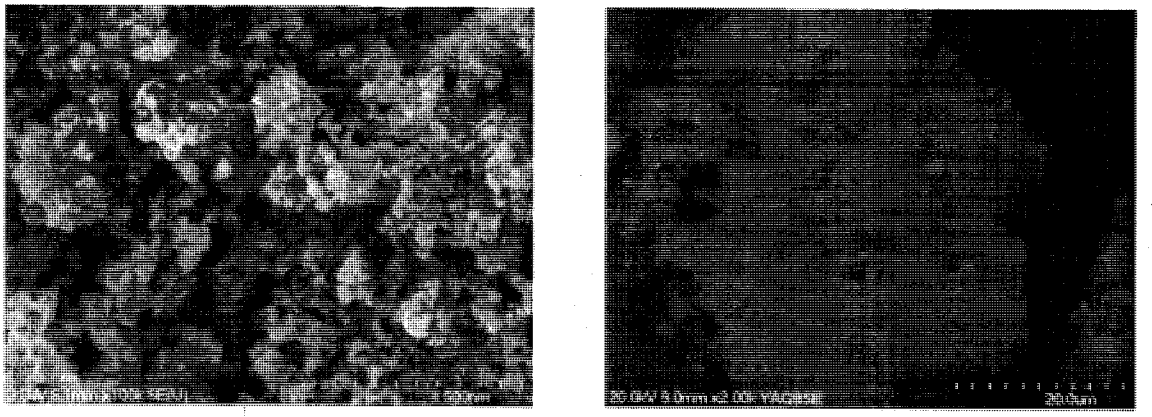

(a) (b)

Figure 4.4 SEM images of test OL-1 (a) Secondary electron detector (b) backscattered electron detector

The presence of bright particles in SEM images and iron peaks in XRD spectra, leads us to the conclusion that some of the injected particles did not evaporate completely. The hypothesis of complete evaporation of iron particles and subsequent formation of these bright balls can be rejected, because of the large dimension of these balls. In R.F. plasma nucleated particles have nanometric size and they are highly agglomerated if no quench gas is used.

In order to remove these micrometric balls it was decided to increase the plate power from 25 kW to 45 kW. Increasing the plate power can produces two opposite effects on particle evaporation. On one hand, the total amount of the energy transferred to ionized gases increases. On the other hand, increasing the temperature of the plasma gases will increase its velocity, hence; the residence time of particles in plasma is decreased.

Increasing plate power from 25 to 35 kW did not result in any major differences in XRD spectra. Same peaks with same intensities were obtained. SEM images of test OL-2 also shows the presence of the same balls, with the same diameter range (Figure 4.5).

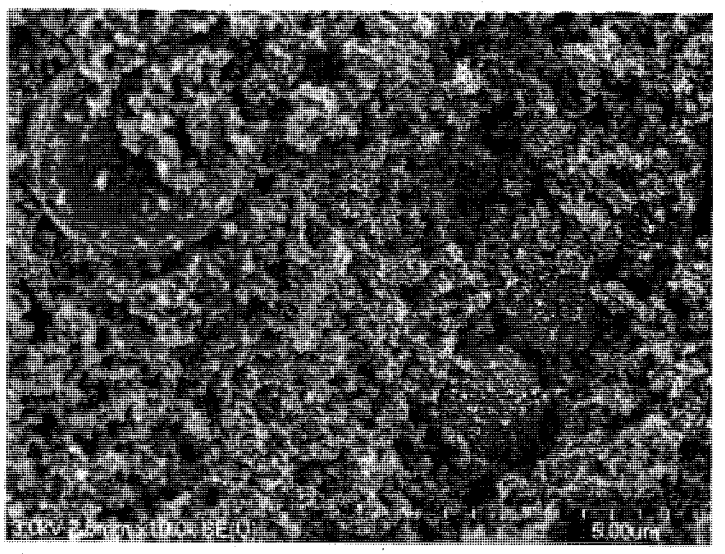

Figure 4.5 SEM images of round micrometric balls (test OL-2)

In test OL-3 it was decided to increase the plate power to 45 kW. The produced powder burned as the reactor was separated from the torch and the produced powder exposed to air. XRD results showed the formation of Fe_2O_3. Fe_2O_3 named as hematite (JCPDS 079-0469) and it has intense peaks which matched very well with the obtained spectrum of XRD in Figure 4.6. Graphite formed during the formation of iron carbide is very stable and the peak of graphite is seen at 24°. This test was reproduced with the same results. Fast oxidation of the produced powder obliged a change in the liquid precursor with no oxygen atoms.

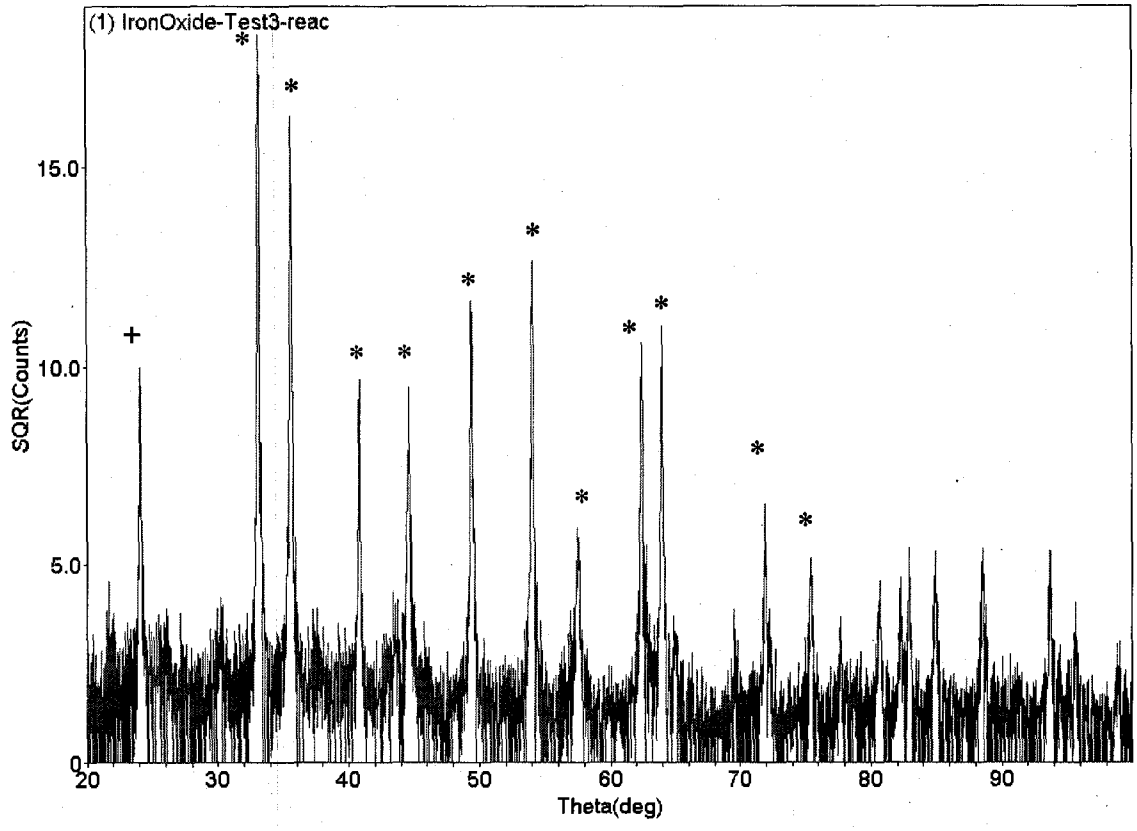

Figure 4.6 Peaks of OL-3

*** hematite, + Graphite**

4.2.5. Hydrocarbon precursor

In order to investigate the effect of the oxygen in the system, liquid containing oxygen was replaced with a mineral oil which is a mixture of different paraffins. The conditions of test ML-1 are the same as OL-3 except that the liquid was replaced with 150 ml of mineral oil. In this test no oxidation at the end of the experiment was observed. XRD results shows that no iron oxide was formed (Figure 4.7). However, some of the injected iron particles did not convert to iron carbide. Further increase of the plate power to 55 kW in test ML-2 did not eliminate pure iron particles in the produced powder.

In Table 4.2, experimental conditions of test ML-1 and ML-2 are presented. The only justification of particle protection against oxidation could be the coverage of particles with

amorphous carbon or graphite. In the case of injection of oxygenate liquids, the oxygen may consume carbon to form CO or CO_2. If it is assume that all of the oxygen atoms react with available carbon atoms in the system and form CO, then the Fe/C would be 0.5 for OL tests and 0.06 for ML tests. So the amount of available carbon for iron carbide formation and particle covering was increased by a factor of 10.

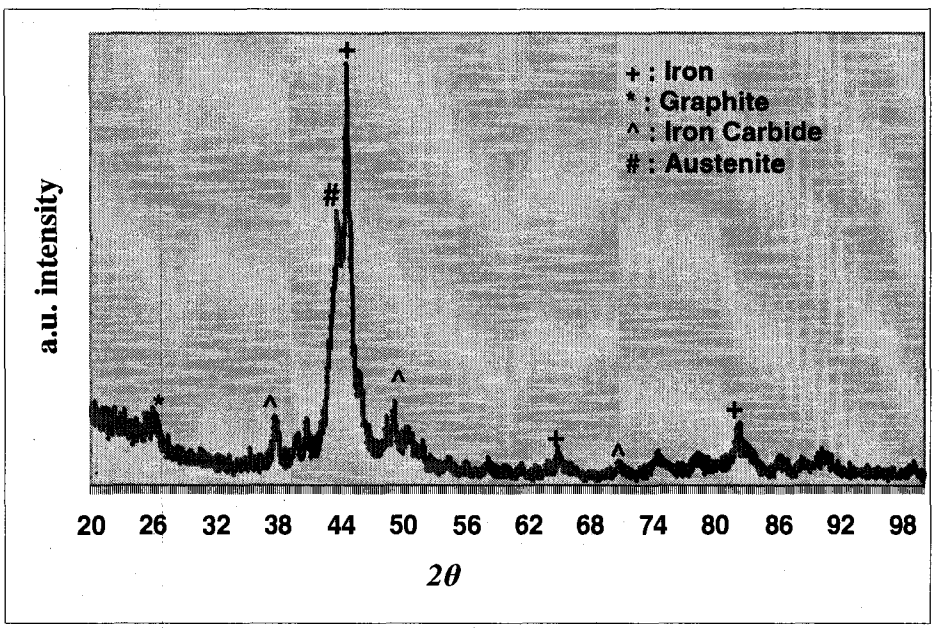

Figure 4.7 XRD results of produced iron carbide powder

Table 4.2 Experimental condition of ML tests

	Tests Number	atomizing gas L/min (STP)	Precursor		Plate Power kW	Injection rate ml/min	Fe/C molar ratio
			Fe	Mineral oil			
Effect of Plate power	ML-1	Ar: 10	20 g	100 ml	45	10	0.06
	ML-2	Ar: 10	80 g	400 ml	55	10	0.06
Effect of Fe/C	ML-3	Ar: 10	15 g	100 ml	45	3	0.045
	ML-4	Ar: 10	30 g	100 ml	45	3	0.09

As mentioned earlier in this chapter, preliminary tests were designed to investigate the qualitative effects of plasma parameters on iron carbide production. In the section, some of the restrictions are mentioned when choosing the composition of feed for suspension injection. By trial and error it was found that the maximum Fe/C molar ratio (without clogging problems) in the probe was about 0.09. This ratio is far from the stoichiometric ratio of cohenite, in which Fe/C is equal to 3. Using this amount of excess carbon can be justified for two reasons.

First, as seen in the thermodynamic analysis, some of carbon atoms will react with hydrogen and form light hydrocarbons. Secondly, it was shown that a certain amount of free carbon is needed to form a protective layer around the produced nanoparticles, or else they will react with oxygen.

Two other tests (ML-3 and ML-4) were designed to investigate the effect of Fe/C. The experimental conditions of these two tests are listed in Table 4.2. XRD and SEM results did not show any significant difference between the two tests results. These results were also the same as the outcome obtained earlier in tests ML-1 and ML-2. These conclusions will be discussed further in the next section.

4.2.6. Discussions

In this chapter it was shown that the formation of iron carbide is feasible thermodynamically in a plasma reactor. The temperature of iron carbide formation is between 2000 and 2300 K. Two different liquids for the suspension preparation were tested. In case of oxygen containing liquid, the produced particles may rapidly oxidize as they are exposed to air. Based on thermodynamic equilibrium results, consumption of carbon by formation of CO is the plausible reason for oxidation of the produced powder. One hypothesis for this rapid oxidation is that as carbon atoms are consumed by CO formation, there is not enough carbon in the system to completely cover produced iron or iron carbide particles. This hypothesis has been validated further when liquid containing oxygen was replaced by mineral oil. It was shown in section 4.2.5 that particle oxidation never happened when mineral oil is used.

Increasing the plate power to 55 kW in tests with mineral oil as the precursor,did not cause powder oxidation. Plate power variation did not change the morphology of the produced powder and XRD peaks corresponding to pure iron did not disappear even when the power increase up to 55 kW. As mentioned in section 4.2.4, increasing the plate power can produce two opposite effects. It can increase temperature of the reactor, but also reduce the residence time of particle in the reactor. The effect of this parameter will be discussed in detail in next section, in terms of a factorial design.

One of the limitations of liquid injection is the concentration of solid in the liquid. It was shown in section 4.2.3, that iron concentration in the liquid cannot be more than 0.33 g/ml. Otherwise, this will cause probe clogging. Converting this ratio to molar ratio (Fe/C = 0.09) a deviation from the stoichiometric molar ratio of cohenite (Fe/C = 3) is noted. Changing the molar ratio of iron to carbon from 0.045 to 0.09 did not change the composition of produced powder, nor their morphology. One justification for this observation is that the range of molar ratio change is far from stoichiometric ratio of iron carbide. For this amount of excess carbon, a small change in Fe/C molar ratio cannot affect the results significantly.

4.3. Suspension injection: statistical analysis

4.3.1. Objectives

In previous section it was shown how liquid injection method can be used to synthesize nanometric iron carbide. Preliminary results showed that to prevent oxidation of the produced powder, the amount of oxygen in the reactor must be controlled. Effects of some plasma processing parameters were also studied. In previous section the effect of only one factor was investigated while other factors were kept constant. The effect of parameter's interaction will not be observed by this method.

In this section, factorial design was used to obtain more reliable and complete results about the effect of each processing parameter, the experimental error and the possible interaction between parameters. As mentioned earlier, factorial design is a robust method in earlier stage of experimentation and it is widely used in factor screening experiments. More precisely, the objectives of this section are to find out the effects of plasma processing parameters on the extent of iron to iron carbide conversion and also their influence on the morphology and size of the produced parameters.

4.3.2. Determination of 2^3 design levels

As described in section 3.6, for a reliable factorial design the high and low level should be as far as possible in order to minimize the effect of possible noises. To do this, a number of experiments were run to find two operational extremes for each factor.

Possible effects of plate power on nanoparticle production are already mentioned in section 4.2.4. Maximum operational plate power for a Tekna PL-50 torches is 60 kW. Power setting of 25 and 55 kW was selected as the two levels for this factor. For plate power below 25 kW, the plasma became unstable because of high flow rates of introduced gases.

Proulx *et al* discussed the effect of injection rate on complete evaporation of particles (Proulx, P. et al., 1987). They argued that high injection rate may cause local cooling of the plasma by cold injected particles which results in incomplete evaporation of the injected particles. Preliminary results have shown that some of the injected iron particles were not

evaporated during synthesis. Hence, the injection flow rate was added as a statistical analysis factor.

In section 4.2.3 the minimum injection flow rate for a continuous injection without probe clogging was reported equal to 5 ml/min. To select high level for injection rate, the recommendation of Proulx *et al* (Proulx, P. et al., 1987) for 10 g/min injection was used.

The third parameter for our factorial design is the probe position. Guo *et al* in their study for synthesis of nanometric silicon carbide reported that by increasing the distance between injection probe tip and plasma fireball the conversion of silicon to silicon carbide increases (Guo, J. et al., 1997). SiC forms at high temperature, about 3000 K, and from their experimentation results they concluded that by increasing the injection distance from the plasma fireball, they increased the residence time of particles in hot regions.

In this work this distance is increased to see its effect on initial iron evaporation. For low level z = 65 mm was chosen. At this distance, the probe tip was placed in the center of the copper coil, which was assumed near the plasma fireball. To determine the high level, the distance was increased gradually. For z greater than 76 mm the plasma became unstable when using 25 kW as plate power. Unstable plasma condition is also reported in the work of Guo *et al* when they increased the distance of injection probe.

Experimental parameters and their high and low levels for factorial design are shown in Table 4.3.

Table 4.3 Levels and parameters for factorial design

Parameters	Coded Factor	Low level (-)	High level (+)
Plate Power (kW)	A	25	55
Injection rate (ml/min)	B	5	10
Probe Position (cm)	C	6.5	7.5

Based on these factors and levels a 2^3 factorial design was made with duplicated tests to improve the reliability of statistical analysis. Experimental conditions of these tests are shown in Table 4.4. These tests were performed in random order to minimize the possible influence of other variables on the statistical analysis. Other operational factors such as gases flow rate and pressure are same as test OL-1.

Table 4.4 2^3 factorial design

Test Number	A	B	C	Run Number	Number of replicate
S-1	+	+	+	6	0
S-2	+	+	-	3	1
S-3	+	-	+	8	0
S-4	+	-	-	2	1
S-5	_	+	+	1	0
S-6	_	+	-	7	0
S-7	_	-	+	4	0
S-8	_	-	-	5	0

4.3.3. Characterization

4.3.3.1. XRD results

Jade 6.0 software can perform a semi-quantitative analysis based on the intensity of some of the most intense peaks of XRD spectra. This semi-quantitative analysis is different from the Rietveld analysis, in which the whole spectrum is simulated and can be used as a quantitative analysis.

Results of semi-quantitative analysis are shown in Table 4.5. In this table replicated tests are marked with a (R) beside the main experiment number.

In this table the conversion is calculated based on total injected iron and by using the following equation:

$$conversion\% = \frac{Iron\ carbide\%}{Iron\% + Austenite\% + Iron\ carbide\%}$$

In this equation it is assumed that all the converted iron is in the form of pure iron, austenite or iron carbide. This assumption is verified using qualitative XRD analysis in which no other iron containing molecule was found. XRD spectra are all similar to that of Figure 4.7, the only difference relates to the intensity of some peaks.

Table 4.5 XRD semi-quantitative analysis

Test No / Phase	S-1	S-2	S-2(R)	S-3	S-4	S-4(R)	S-5	S-6	S-7	S-8
Iron Carbide %	45.8	46.1	44.9	49.5	46	48	49.7	50.5	51.1	50.8
Iron %	31.5	31.4	33.4	24.6	30.9	28.6	24.9	24.3	24.4	25.5
Graphite %	11.6	11.9	12	14.8	12	10	15.2	14.4	12.2	12.3
Austenite %	11.2	10.6	9.7	11.1	11.1	13.4	10.2	10.8	12.3	11.9
Conversion%	65.2	65.7	65.9	64.1	65.0	65.7	64.6	65.2	66.1	66.2

XRD spectra can also provide the crystallite size by using Scherrer equation. To use this equation a completely separated peaks, which has no overlapping with other peaks were selected .

The Scherrer equation is:

$$t = \frac{0.9\lambda}{B\cos\theta}$$

Where:

t : crystallite size (nm)

λ : wave length of radiation (nm)

B : peak breadth in radians

θ : Bragg angle

The only fully separated peaks in Figure 4.7 are at 38° (iron carbide) and 65° (iron). Crystallite size obtained for these two peaks are 25 ± 9 and 35 ± 7 nm respectively averaged on 5 measurements. As these values are very close and overlapping it will be difficult to used TEM and HRTEM pictures and identify the nature of particles based on their size.

4.3.3.2. TEM and HRTEM

Morphology and size of produced particles can be studied by using TEM images. There is no variation between images of different tests. Hence, images of test S-5 were chosen for further investigation on morphology and size of different particles produced in one test.

Figure 4.8 (a) shows TEM image of test S-5 taken by Hitachi H-7500 microscope. This TEM image cannot show the size of the particle and its morphology because it seems that particles are covered with a layer of other phase (the nature of this layer will be determined later by HRTEM images). However, blurred black particles with 40-50 nm in diameter can be distinguished in this image. Figure 4.8 (b) shows other TEM image of the same test taken by Jeol 2010F. In this image the small particles are seen more clearly. The particles size varies between 10 to 40 nm.

These two figures, shown that some particles are brighter than the others. It cannot be that these particles have different nature. The difference in color can be originated from overlaying effect. There is a chance for particles to be placed over each other. These points will transmit less electrons hence they look like darker.

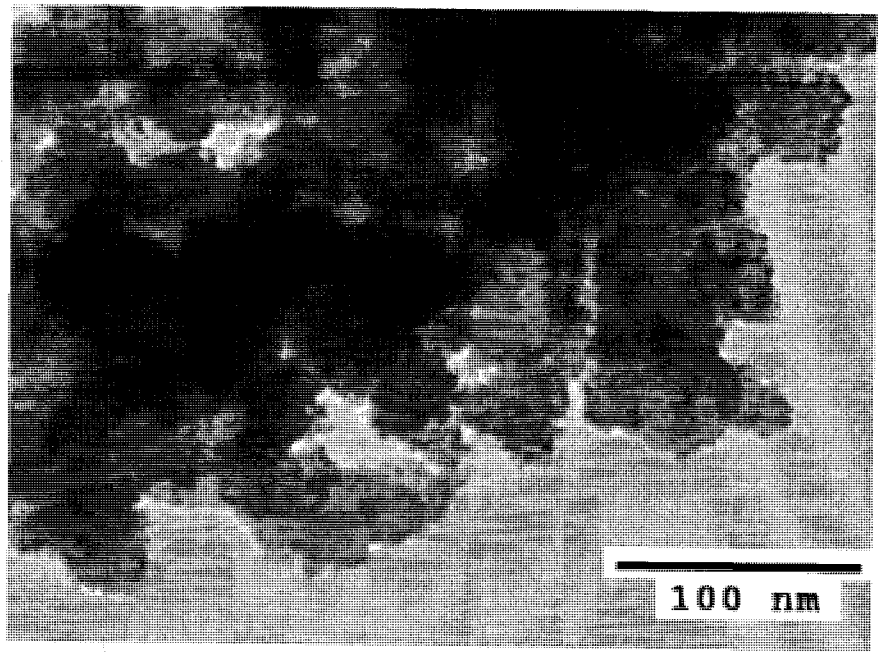

(a)

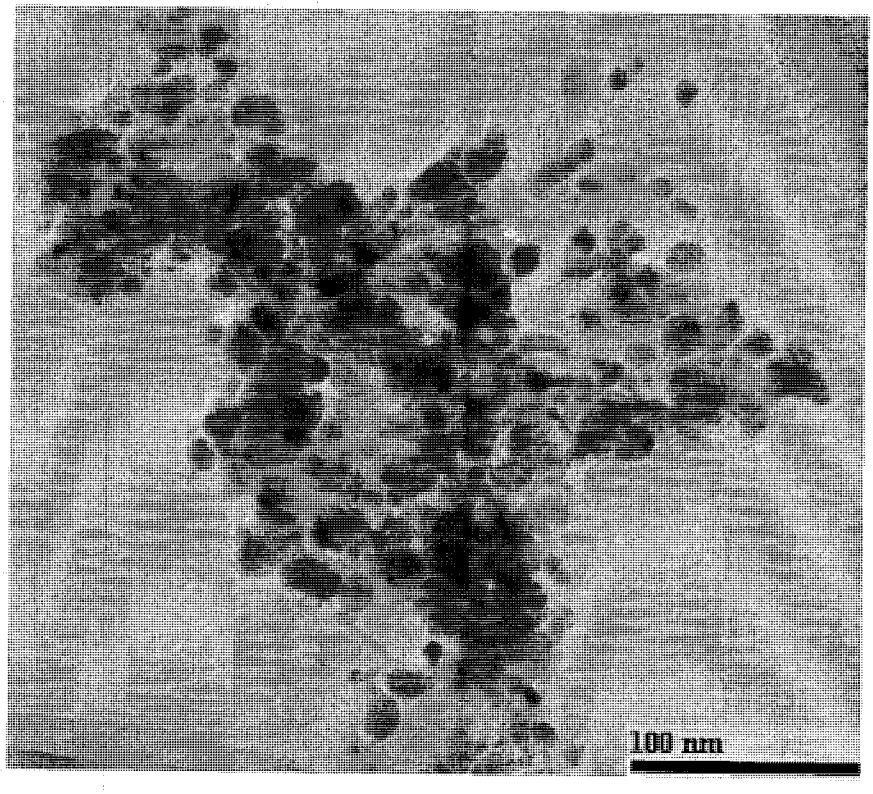

(b)

Figure 4.8 TEM images of test S-5

Some HRTEM images are taken in order to evaluate the chemical composition of different particles as determined by interplanar spacing we have taken. In Figure 4.9 some parallel planes which form a U–shaped structure in the picture are observed. The interplanar distance, calculated in one region (white circle) is equal to 0.36 nm.

Although interplanar spacing of bulk graphite for (002) plane is 0.338 nm, the d-spacing between 0.36 to 0.40 nm is reported in the literature when rare graphene layers form beside a large amount of amorphous carbon (Jäger, C. et al., 2006)

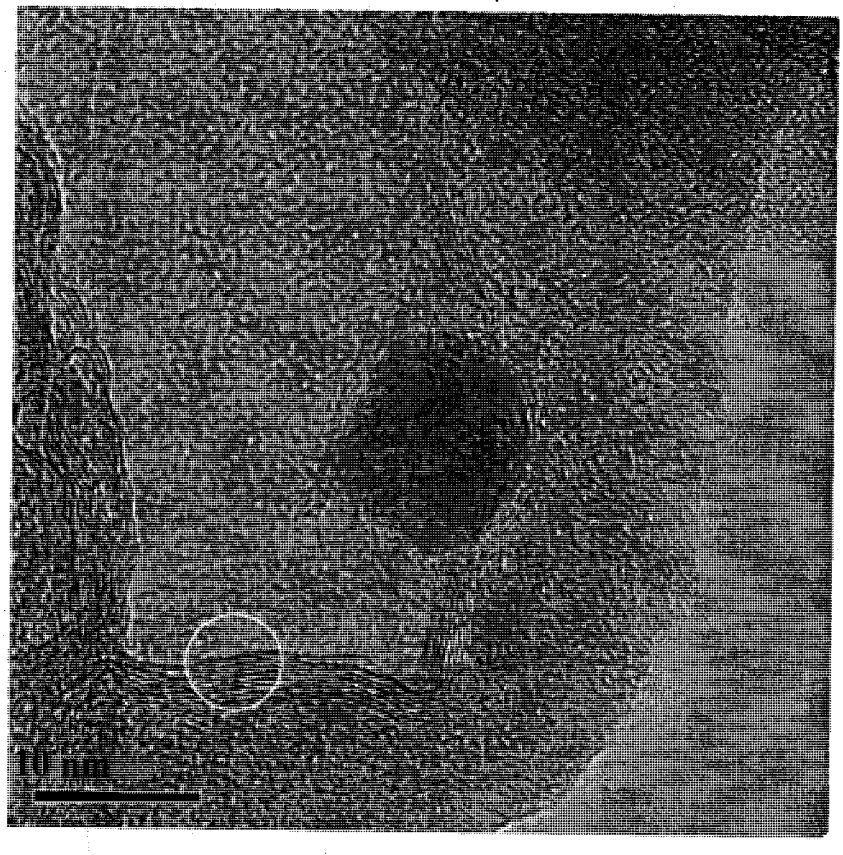

Figure 4.9 Graphite layers

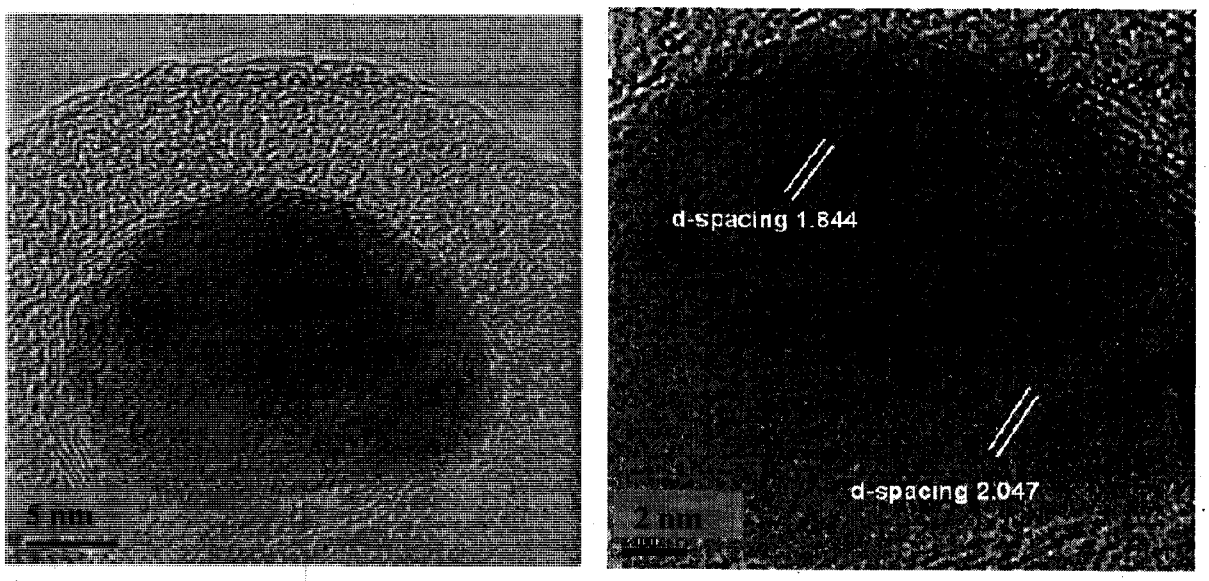

(a) **(b)**

Figure 4.10 HRTEM image of iron carbide nanoparticle

In Figure 4.10 (a) a single particle with a diameter of about 20 nm is shown. Some parallel lines are seen very close to the particle surface. The interplanar spacing of these planes is again 0.36 nm and they are identical to graphite planes. Most part of particle surrounding has no specific crystalline orientation; hence, it consists of amorphous carbon. Other characteristics of this particle are that the graphite layer is not regular and it is not covering the particle completely.

In Figure 4.10 (b) the interplanar spacing of crystalline plane inside the same particle was measured by means of a computer-aided-image analyzer. A two d-spacing of 1.844 and 2.047 nm, were formed and match well with (002) and (113) planes of iron carbide (JCPDS 089-2722). It is worth noting that 2.047 nm can also represent iron interplanar spacing, but the 1.844 nm belongs only to iron carbide and it confirms us that the observed particle is an iron carbide particle.

4.3.3.3. TGA analysis

Thermogravimetric analysis determines the amount of total carbon in the produced powder. In this analysis, the obtained powder was located in air to make carbon atoms react

with oxygen and leave the sample. The weight change of the sample can be used to calculate the total amount of carbon in the initial powder. It can also give some information about existing phases in the powder. In this study, the produced powder is heated in an air flow from ambient temperature to 1000°C with a temperature ramp of 10°C/min.

Figure 4.11 shows TGA analysis of pure iron that we used as starting material. This diagram serves as a reference. As seen in this figure, the main mass gain begins at 300°C and continues to 600°C. If all iron atoms oxidize completely and convert to iron oxide mass gain of 48% is obtained; hence, this diagram showed that was not reached completely. Incomplete oxidization can also be seen by the increasing trend at high temperatures.

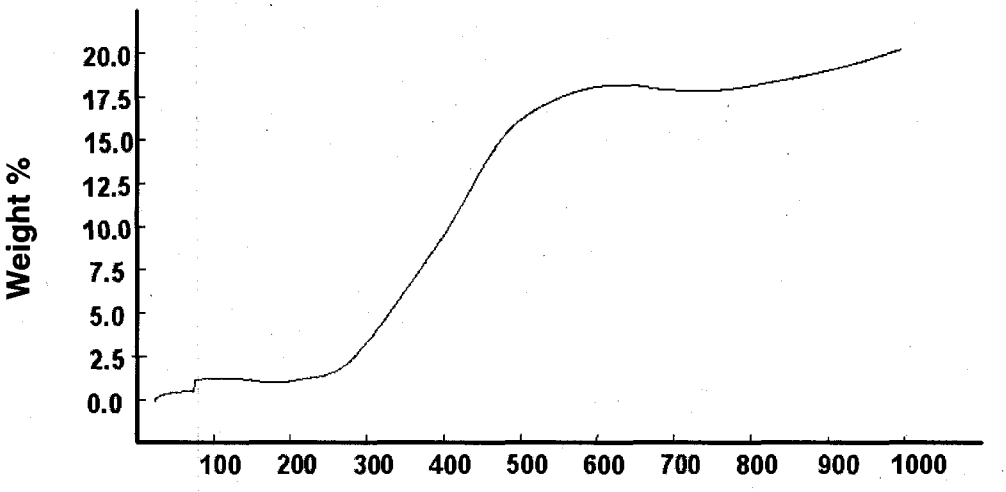

Figure 4.11 TGA result of pure iron

The same set up and the same parameters for the iron carbide oxidization were used. Figure 4.12 shows the TGA curve obtained by heating produced the powder of test S-5 in air up to 1000°C.

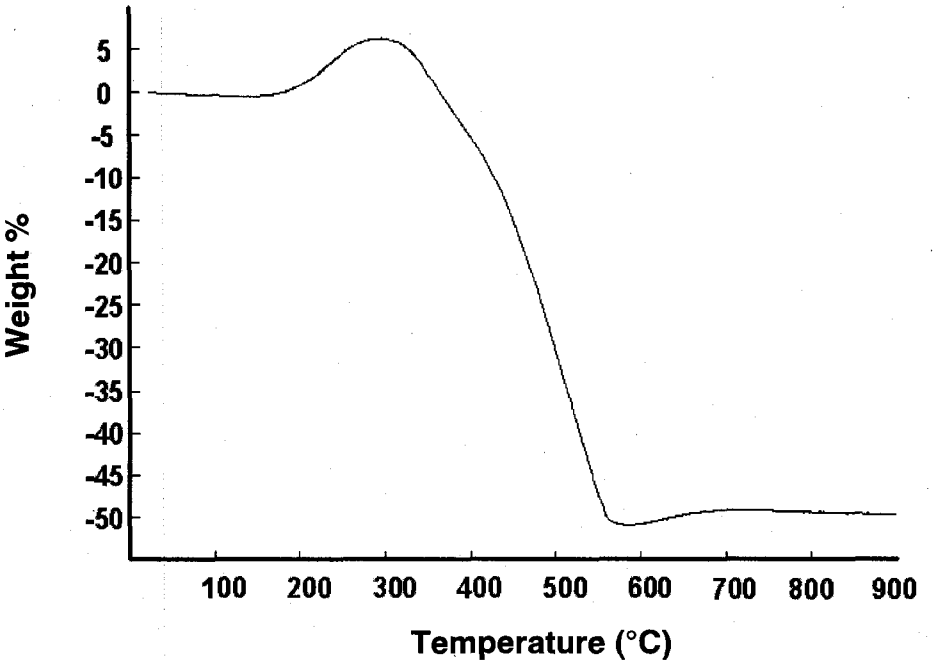

Figure 4.12 TGA of test S-5

It is seen in this experiment that the weight change stops after 900°C. This fact shows that the iron oxidation mechanism and its onset in the presence of large amounts of carbon might be different from that of pure iron. Total weight loss in this experiment is about 50%. If it is assumed that iron oxidation is complete (horizontal curve tail after 700°C) and that only iron oxide is obtained at the end of the experiment in form of Fe_2O_3 then, the initial amount of iron in the powder was 13.8% and the total amount of carbon was 86.2%.

Considering the initial Fe/C mole ratio which was 0.06 (wt.% Fe = 21.8), the weight percent of iron increased. This increase in weight percent of iron could be due to consumption of carbon by formation of CO and CO_2 in the plasma reactor because of the air leaks.

4.3.4. Statistical analysis

2^3 factorial design was shown in section 4.3.2 To analyze the results of this factorial design an ANOVA table was constructed by using Design Expert 6.0.1 software. Complete ANOVA table is shown in Table 4.6.

Table 4.6 ANOVA table

Source	Sum of Squares	DF	Mean Square	F Value	Prob > F
Model	22,72	7,00	3,25	0,94	0.5227
A(Power)	3,72	1,00	3,72	1,07	0.3271
B(Injection rate)	0,25	1,00	0,25	0,07	0.7942
C(P.P)	0,67	1,00	0,67	0,19	0.6710
AB	12,36	1,00	12,36	3,57	0.0914
AC	3,72	1,00	3,72	1,07	0.3271
BC	1,91	1,00	1,91	0,55	0.4761
ABC	0,04	1,00	0,04	0,01	0.9213
Residual	31,15	9,00	3,46		
Lack of Fit	16,37	4,00	4,09	1,38	0.3589
Pure Error	14,78	5,00	2,96		
Cor Total	53,86	16,00			

To construct this table the effect of each factor was considered with all possible interactions for the conversion of iron to iron carbon (Fe_3C)

The last column of this table shows the *p-value*. A factor is significant if the *p-value* value is less than 0.05 (considered as the level of significance). As seen in this table, none of the selected parameters are significant in the ranges used in this experimental analysis. In other word, the probability that the selected parameters with selected levels make a significant change in the result is far less than 5%. The mean value of conversion for these tests is 65.37 and standard deviation value is 0.22.

The second row of the table shows the chosen model for this analysis, and as seen, this model is not significant. The model is a mathematical equation which includes main operational parameters and it is used to predict the final response when the value of one parameter is changed. The model used in this analysis is a linear one in form of:

$$\text{Conversion} = a_0 + a_1A + a_2B + a_3C + a_4AB + a_5AC + a_6BC + a_7ABC$$

In which a_i is constant and A, B, C ... shows factors or their interaction (e.g. AB is not the product of factor A and factor B, it means the interaction of A and B).

The objective of this experimental work was to find information about the mechanism of nanoparticle formation and to determine factors which may affect conversion of iron to iron carbide. Since in this does not seek an empirical model for iron to iron carbide conversion, no other further model were tested. The search for another model implies the use of combination of these parameters in nonlinear form to obtain a significant one.

4.3.5. Discussions

In chapter 3, two opposite effects of the plate power on injected particle evaporation was considered. Increasing plate power will increase the temperature of ionized gases as well as the volume of plasma gases; hence, it makes the evaporation of injected iron particles easier. Meanwhile, as the temperature of gases increases, the velocity of plasma gases increase and the residence time of particles in the hot plasma zone decreases. This can reduce the total amount of energy transferred to particle, and as a result; particles may pass the hot zones without complete evaporation.

Statistical analysis showed that changing plate power from 25 to 55 kW did not change significantly the extent of conversion. It may be argued that, even at 25 kW the transferred energy to particles was sufficient to evaporate most of them. The presence of unevaporated particles might be due to some preferential trajectories in the plasma zone where particles pass without being exposed to high temperatures.

Probe position cannot affect the residence time of particles in the chosen range. The only possible effect of probe position could be on changing the trajectories of injected particles in plasma zone. This parameter did not change the conversion of iron to iron carbide as well. No reliable explanation is found for this observation; however, the tiny difference between low level and high level of this parameter which was imposed by plasma stability need to be considered.

Finally, reducing injection flow rate to its minimum did not change the conversion. It concluded that even at a high level (10 ml/min), the injection flow rate limit was not reached. The effect of injection flow rate on produced powder cannot rule out completely. All that must be said is that it did not have a significant effect in the chosen range. The work was

conducted to see whether the injection rate can improve the conversion, and it was shown that the injection rate has no significant effect even when it is set at a minimal level.

4.4. Solid injection technique

4.4.1. Objectives

In previous sections it was shown that one of the limitations of liquid injection technique was that iron to carbon ratio in injected precursor was far from the cohenite stoichiometric ratio. Statistical analysis of liquid injection technique also showed that none of the processing factors had a significant effect on iron to iron carbide conversion.

The objective of this chapter is to investigate the effect of Fe/C molar ratio in iron carbide synthesis. Through the solid injection method, this ratio can be changed up to the stoichiometric ratio of iron carbide.

Another unsolved problem from the previous sections is whether the conversion is limited by the amount of energy transferred to particles or by chemical reaction rate. Limitation by the amount of energy transferred to the particles means that the plasma zone is not hot enough or that the residence time is too short. These two factors may let the particles to leave the hot zones before complete evaporation. Presence of some bypasses may also help particles to traverse the plasma region without complete evaporation.

Chemical reaction limitation means that iron particles evaporate completely but the reaction between iron and carbon atoms are not fast enough or that there is deficit of one of reactants in certain regions. The other possibility could be the faster condensation of iron particles than iron carbide reaction. In this case the iron particles nucleate and agglomerate before iron carbide formation.

Another objective of this section is changing the diameter of injected iron particles in order to explain the above questions. If reducing the diameter of particles has a significant effect on iron evaporation and iron carbide conversion it means that the amount of energy transferred to the particles and/or the residence time of particles in the high temperature regions were the limiting steps.

Evaporation of larger particles as done for smaller particles, shows that the conversion extent is limited by the reaction kinetic. It is also worth noting that the reaction is not limited by thermodynamic equilibrium. As seen earlier in section 4.2.2, all iron atoms react with carbon containing molecules or radicals to form iron carbide if the system reaches the equilibrium state.

4.4.2. Operational conditions and results

A numbers of experiments are designed for this section to achieve objectives cited in previous section. Table 4.7 shows experimental conditions of these tests. In all these tests, Ar is used as central gas with 23 l/min (STP) flow rate and precursors are pure iron powder and acetylene. Power is held constant for all these tests at 45 kW.

Table 4.7 Operational condition, powder injection mode

Test No.	Injected iron powder diameter (μm)	Precursor injection rate (g/min)	Sheath gas composition	Radial Ar l/min (STP)	Conversion %
P-1	+45	4.6	H_2, 10 slpm	0	12
P-2	+25	3.4	H_2, 10 slpm	0	49
P-3	1-3	3.3	H_2, 10 slpm	0	55
P-4	1-3	3.3	He, 50	0	59
P-5	1-3	4.3	He, 50	30	46

Effect of injected particle size

Tests P-1 to P-3 are designed to investigate the effect of injected particle diameter on conversion. The conversion of iron to iron carbide is calculated by using results of semi-quantitative XRD with the same steps described earlier in section 4.3.3.

In test P-1, 72% of injected iron particles were accumulated on the bottom of the main chamber. This powder has a silver color and it is assumed to be free of iron carbide particles. These particles were not entrained by the gas stream to the auxiliary chamber because of their mass and consequently their huge momentum. This justification is approved by results of P-2 and P-3 test where no powder was accumulated on the bottom of the main chamber.

Figure 4.13 shows the extent of iron to iron carbide conversion versus injected particle size. An obvious increase in conversion can be seen as we reduce the diameter of the injected particle.

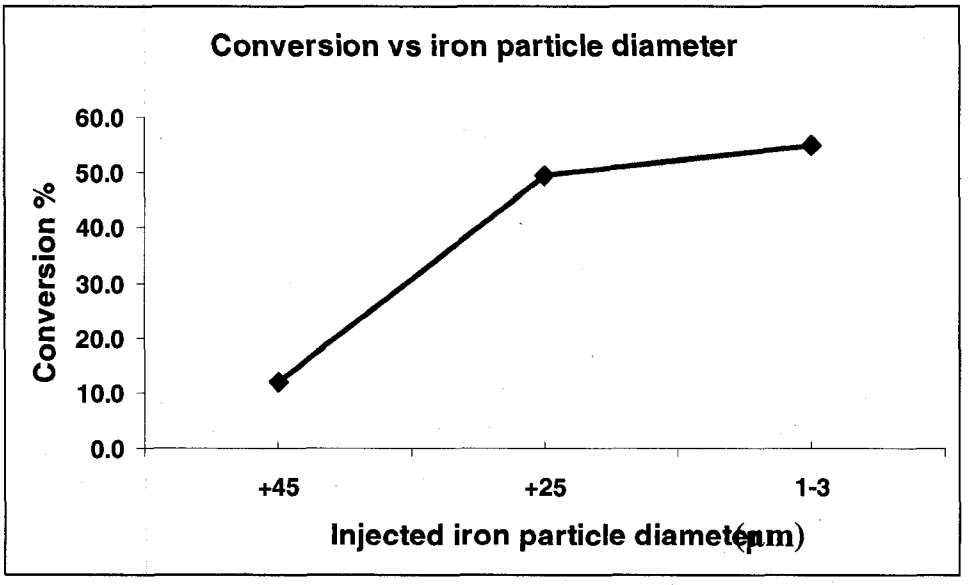

Figure 4.13 Effect of injected iron particle diameter on conversion

Previously, it was argued that one of the limitations for iron to iron carbide conversion was the incomplete evaporation of injected iron particles. Results of this section show that this hypothesis is correct because as the initial iron particle diameter is increased, iron to iron carbide conversion increased. Larger particles have shorter residence time in plasma zone because higher drag force is exerted from gases stream on these particles. At the same time, higher amount of energy must be transferred to these particles to evaporate them completely. Synergetic effect of these two factors results in the possibility for iron particles to pass through the plasma zone without complete evaporation. Figure 4.13 clearly shows that initial iron evaporation has a significant effect on iron to iron carbide conversion.

Effect of Hydrogen

Arabczyk *et al* in their paper found a rate equation for iron to iron carbide conversion (Arabczyk, W. et al., 2004). In their study they used methane, methane/hydrogen or methane/nitrogen mixture at temperatures between 500-580°C which resulted in the synthesis of carburized nanocrystalline iron particles, promoted by K_2O, Al_2O_3 and CaO. They found that the overall reaction is reversible and it can be expressed as follow:

$$3Fe + CH_4 \underset{r^-}{\overset{r^+}{\Leftrightarrow}} Fe_3C + 2H_2$$

This reverse reaction is of first order regarding to hydrogen partial pressure. The rate of the reverse reaction was about one tenth of the forward reaction.

In order to investigate the effect of hydrogen on conversion, hydrogen was replaced in sheath gas by helium in test P-4. Helium is a monatomic gas with specific enthalpy close to hydrogen as it is shown in Figure 2.8. Operational conditions of tests P-3 and P-4, other than sheath gas composition, are held constant for sake of comparison. Iron to iron carbide conversion in test P-4 is 59%, slightly higher than that of test P-3 (55%). The change in conversion is not substantial, and it could be due to small differences in synthesis technique and operational conditions.

Radial injection

Radial injection of a cold gas can rapidly reduce plasma gases temperature, and hence prevent agglomeration of nucleated particles. Proulx *et al* described mathematical equations for particle growth in R.F. plasma (Proulx, P. et al., 1991). In their mathematical model they assumed that all the collisions result in coalescence. The frequency of collisions due to Brownian movement of nucleated particles is proportional to the square root of the absolute temperature. In their modeling study, they found out that injection of radial Ar with 50 slpm flow rate decreases the mean diameter of particles by 25%. Soucy *et al* in their study investigated the effect of 2, 4 and 8 point radial quench gas injection on plasma gases stream (Soucy, G. et al., 1995). They found that if the average velocity of gases exiting a nozzle is above 50 m/s, then the gases penetrate into the hot plasma gas. If the average velocity is below 50 m/s then the cold gas stream will blend gradually with plasma gas downstream.

In this study Ar gas was injected radially into the plasma gas from 12 nozzles perpendicular to plasma gases stream. The injection flow rate is 30 slpm and the average velocity of gases was 80 m/s. Conversion of iron to iron carbide decreased to 46% and more austenite has been formed compared to test P-4. Morphology and size of produced particles will be shown in next section.

4.4.3. Characterization

X-ray diffraction analysis

Figure 4.14 shows XRD spectrum of test P-1. This powder had a black color and it was collected from the main chamber wall. As seen in this figure, XRD peaks are similar to peaks of Figure 4.4 and it may be concluded that the powder contains iron carbide, iron, austenite and graphite. XRD spectra of other tests are not presented here because they were all similar to spectra of test P-1. Conversion of iron to iron carbide is calculated for each test with the semi-quantitative method described earlier in section 4.3.3.1 and it is shown in Table 4.7

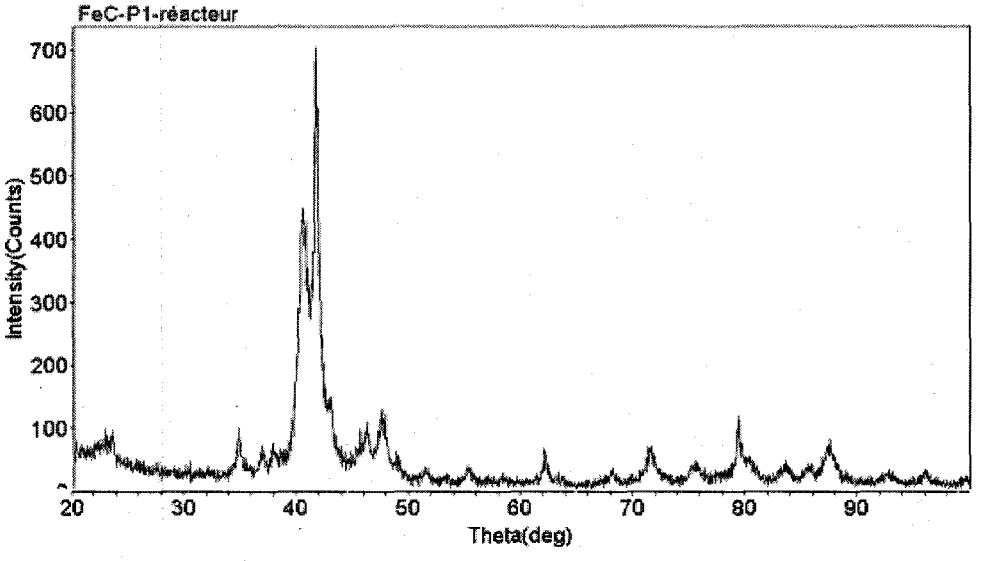

Figure 4.14 XRD spectrum of test P-1

TEM and HRTEM images

Several pictures have been taken from powders synthesized using the solid injection technique. All the pictures had similarities and the images of test P-4 is selected based on its clarity. Figure 4.15 shows a TEM image of this test and it is taken by Hitachi H-7500 TEM microscopy with 20K magnification.

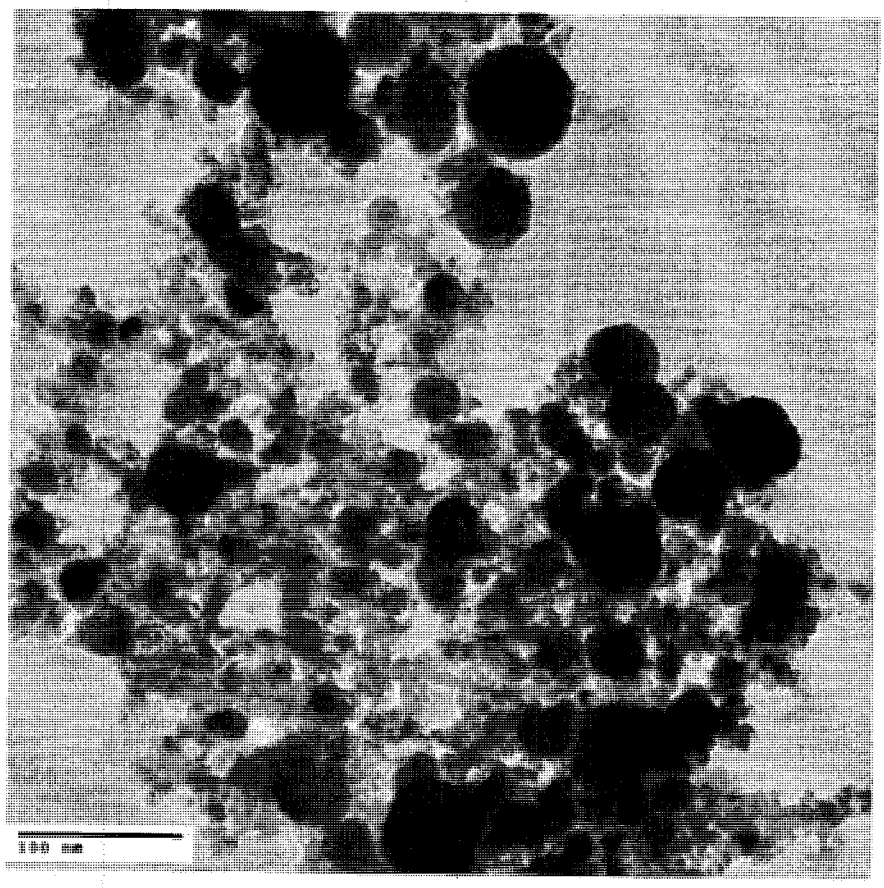

Figure 4.15 TEM image of test P-4

The size of particles in this picture is in the range of 10-70 nm. As it can be seen in this picture, particles have a shell-core structure. Shell-core structure means that these particles have dark interior part which is covered with a bright thin layer. This structure was obtained by other researchers as shown earlier in Chapter 2. In this case, the core probably consists of iron or iron carbide and the shell is probably amorphous carbon or graphite. These claims will be justified using HRTEM images.

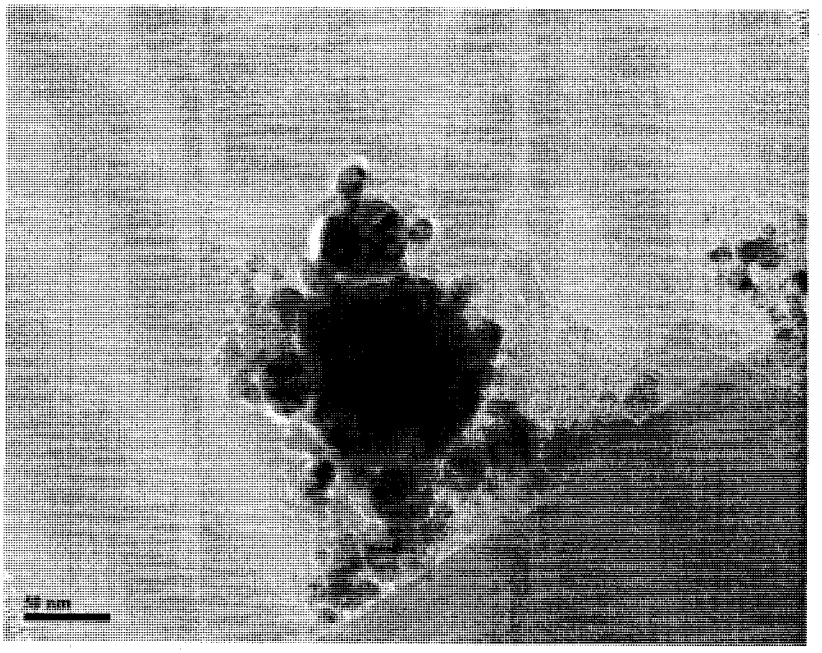

Figure 4.16 TEM image of a particle test P-4

Figure 4.16 shows a low resolution image of a cluster of nanometric particles. This image was taken by a JEOL 2010 HRTEM. The diameter of the greatest particle is about 100 nm. The interface of this particle with the 50 nm diameter particle above it is shown in Figure 4.17. Interplanar spacing is measured for two regions of this particle. Measured values were 2.02 Å and 2.12 Å for region "a" and "b" respectively. These two interplanar spacing match very well with (211) and (102) planes of Fe_7C_3 with JCPDS number 017-0333. In the region between two particles some crystal planes are observed but they are not parallel and the interplanar spacing could not measured by means of the image analyzer. Other d-spacing values measured from other HRTEM images were between 2.10 and 2.15 Å. Only iron carbide phases with interplanar spacing in these regions are Fe_2C_5 (JCPDS 036-1248) and Fe_7C_3 (JCPDS 017-0333).

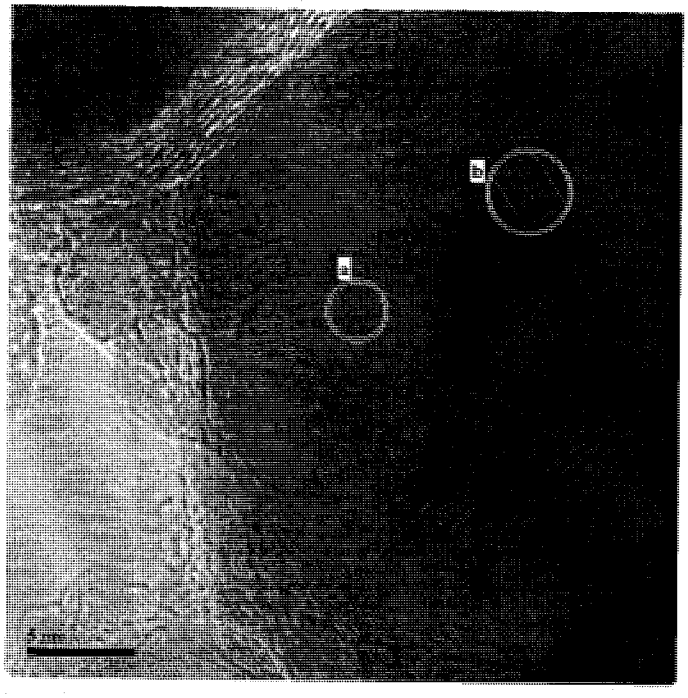

Figure 4.17 HRTEM image of particle shown in Figure 4-14

TGA and BET analysis

Figure 4.18 shows TGA results of tests P-1 and P-2. TGA curve of test S-5 is added for comparison. The temperature increase program used for oxidation in air is the same as that used earlier for TGA analysis of powder synthesized by liquid injection. It clearly shows that the total amount of carbon in the solid injection test is considerably lower than that of the liquid injection test. If it is assumed that all of the iron atoms transform to iron oxide with Fe_2O_3 formula, then it may be stated that the initial powder had 75% of iron atoms by weight and 25% of carbon.

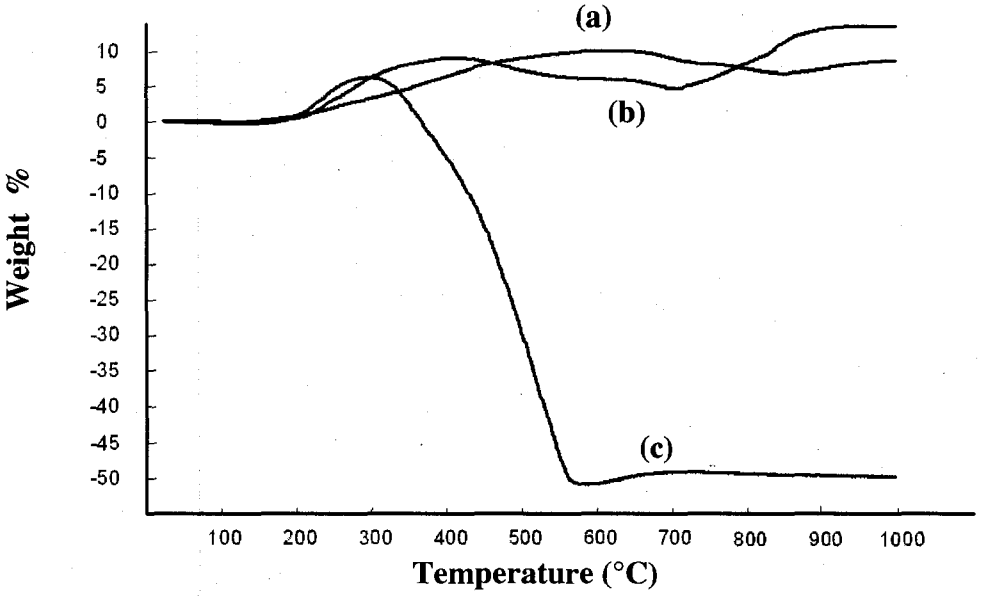

Figure 4.18 TGA analysis (a) test P-2, (b) test P-1, (c) test S-5

Specific area of two sample tests were measured using BET method. Specific surface area of test S-5 was 72 m^2/g and that of test P-2 was 34 m^2/g. Differences in specific surface area could be due to differences in particle size. As the particle size reduces, the specific area increases. TEM and HRTEM images of these two tests did not show a substantial differences in particle size so this difference may be originated from other properties of these powders. TGA analysis of these powders showed that the total amount of carbon for test S-5 is much higher than that of test P-2. The amount of excess carbon that seen in the HRTEM images has an amorphous structure. So the presence of a huge amount of amorphous carbon is at the origin of this difference in specific surface area between test S-5 and P-2.

4.4.4. Discussions

In section 4.3.5, it was argued that the conversion of iron to iron carbide may be limited by two mechanisms. First, the injected iron particles do not reach complete evaporation. This could be due to a short residence time of the particles in the plasma zone, and also because of local cooling of the plasma due to cold precursor injection. The second limiting mechanism could be the low reaction rate between gaseous iron atoms and carbon containing molecules, or radicals.

In the first three experiments in this section, the diameter of the injected particles was decreased. The objective of these experiments was to reduce the required time for complete evaporation of particles and to evaluate its role on total conversion. The obtained results showed that decreasing particle diameter increased the extent of conversion.

In addition to the above results, injection of cold gases into the plasma zone in test P-5 also resulted in a reduction of the iron to iron carbide conversion. These results clearly show that the total energy transferred to the particles in the plasma zone can be one of the limiting steps in our case. Depending on the size of the injected particles, some of them may have evaporated completely and subsequently reacted with carbon atoms to form iron carbide and some larger particles or a agglomerates of iron particles may not evaporate completely and traverse the plasma zone without reaction. Presence of some colder trajectories in the plasma region cannot be ruled out. Particles traversing these regions may not be exposed to high temperatures, hence they will not be evaporated. None of the tests designed in this study can give us information about the role of reaction kinetic on conversion limitation.

One of the possible explanations for the limited conversion of iron to iron carbide after liquid injection method could be the effect of heavy liquid decomposition and required energy on the formation of iron carbide. The hypothesis is that a huge amount of energy is needed for complete decomposition of heavy hydrocarbon, and this could limit the available active carbon atoms for iron carbide formation. In this section we used C_2H_2 which is a simple reactive gas and the resulting conversion was similar to that of the liquid injection technique. This can show that the previous hypothesis cannot explain the main reason of limited conversion in our study.

The result obtained in these two sections can be used to verify some of the possible mechanism of iron carbide production in the plasma reactor. The formation of gaseous iron

carbide is not a possible route because of the crystalline structure of cementite, austenite and ferrite.

There are three sources of carbon atoms in the plasma reactor. In gaseous phase they form free radicals with hydrogen atoms at high temperature and in low temperature they form stable light hydrocarbon molecules. In solid phase they may form soot particles at temperature below 3000 K (Figure 4.2). Other possible source of carbon atoms for iron carbide formation reaction is the carbon atoms dissolved in liquid iron or the carbon atoms adsorbed on the surface of solid iron particles. As mentioned earlier in the literature review section, iron atoms can provide active sites for hydrocarbon adsorption and subsequent hydrocarbon cracking. During these reactions some of the carbon atoms diffuse into the iron matrix and form different iron-carbon alloys. The structure of these alloys depends on the amount of diffused carbon atoms and also on the temperature history of the particle. If the particle is suddenly cooled down, then meta-stable phases like austenite or martensite will be produced. If the cooling procedure is taking place slowly then stable phases such as cementite will be formed.

XRD results obtained in this project did not show martensite peaks, however we cannot rule out the formation of martensite because its peaks are very close to ferrite peaks. To draw a conclusion for mechanism of iron carbide formation one must consider the important fact that in plasma reactor there is a high temperature gradient in the reactor. This temperature gradient has two effects on the chemical composition of produced particles: First, the produced particles are not all exposed to the same temperature zones; hence, they have a different temperature history. Secondly, all particles temperature suddenly decreases and this favors the formation of meta-stable phases.

The reaction of soot particles with solid iron particles cannot be the main mechanism of iron carbide production because of the relatively slow reaction rate between two solid phases. However, this reaction cannot rule out because the small size of these solid particles can improve the reaction rate.

Based on the above discussions the most probable mechanism for iron carbide formation is the reaction between dissolved carbon atoms and liquid iron or the reaction between adsorbed carbon atoms and solid iron nanoparticles. The formation of meta-stable phases like austenite is due to sudden particle temperature drop in the plasma reactor. This sudden temperature drop can also be the cause of incomplete diffusion of carbon atoms into the iron

structure and the formation of ferrite structure. The best indications of this temperature drop are the pictures that were taken by HRTEM. In this chapter the d-spacing of the synthesized particles was slightly different from the literature values and this can be due to the fast formation of crystal structure.

CONCLUSION

The objective of this project was to synthesize iron carbide nanoparticles using an induction plasma reactor. During this project several injection techniques were used to improve the purity of the synthesized iron carbide nanoparticles. Scientific hypothesis were made in each section to enhance the purity of the produced nanoparticles and these hypothesis were tested by specially designed experiments to verify their validity. The objective of each section of this work was to study the effect of plasma processing parameters on the size and purity of the produced powder.

Thermodynamic analysis of the system showed that the production of iron carbide at high temperature is feasible if there are enough carbon and iron atoms in the system. Thermodynamic analysis showed that iron carbide will be formed between 2000-2300 K. Solid carbon formation takes place at about 3000 K and if there is oxygen atoms in the system they will react with carbon atoms to form CO.

The project was initiated by running some preliminary experiments to solve possible technical problems. Other purposes of the preliminary tests were to determine the operational range of important processing parameters and also to find suitable precursor for iron carbide production. In suspension injection technique the main technical problems were to find out a way for homogeneous suspension preparation and to inject the suspension continuously without probe blockage. For precursors used in this work the maximum solid concentration in liquid was 0.33 g/ml and that the injection rate could not be below 5 ml/min.

Two liquid precursors were used as the liquid medium in suspension and also as carbon donor precursor. First, a mixture of butanol and glycerol was used as liquid medium An increase of the plate power above 45 kW produced powders that oxidized quickly as they were exposed to air. The liquid career was changed with mineral oil which did not contain oxygen atoms. A replicate test with the same experimental condition, as the test with oxygenate precursor, showed that the produced powder are stable in air even after a long time exposures. This result, and the fact that oxygen atoms react with carbon atoms to form CO, showed that to form iron carbide and to protect it against oxidation the presence of oxygen atoms in the system must take into account.

In the preliminary tests iron carbide particle was produced with a size range between 10-100 nm and iron to iron carbide conversion was about 50%. SEM and TEM images showed that besides nanometric particles some of the particles are in the range of 1-5 μm and their shape was the same as the initial iron particles injected as precursor. XRD results also confirm the presence of pure iron and austenite in the synthesized powder. Based on these results one the probable hypothesis was that the injected iron particles did not have enough time in the hot plasma zone to evaporate completely.

To improve iron to iron carbide conversion it was decided to study the effect of processing parameters on the extent of conversion. A 2^3 factorial design was run with plate power, probe position and injection rate as parameters. Statistical analysis of this run showed that none of the chosen factors can significantly influence the conversion of iron to iron carbide. These results show that we have to change the range of parameters or that their effect may be cancel out by their opposite effects. For example, as the plate power increases the total amount of energy transferred to ionized gases is increased and particles in hotter ionized gases evaporate faster. Meanwhile, when the injected gases are hotter, the entrained solid particle will traverse the hot regions faster.

Iron to carbon molar ratio in liquid injection technique cannot be above 0.09. Cementite which is the most stable iron carbide has iron to carbon molar ratio equal to 3, hence, liquid injection did not fallow iron carbide stoichiometric ratio. Solid injection technique, allowed introduction of reactants with ratios near that of iron carbide to prevent formation of excess free carbon. The results showed that this technique increased iron carbide composition in the produced powder from 10 to 45%.

In order to investigate the effect of particle size on conversion the initial size of the injected iron particles was changed. Results showed that, the injection of coarser particles decreased iron to iron carbide conversion. This result confirms the hypothesis that the limiting step for iron to iron carbide conversion is the incomplete evaporation of injected particles. Injection of very small iron particles may introduce some coarse particle as impurities or agglomerates in the initial powder Particles may also form clusters during the flight. These factors could be the sources of iron impurities in the produced iron carbide.

The recommendation for future work is to design experiments in which the particles residence time may be increased significantly in the plasma region. The effect of other processing factor like reactor pressure may also investigate to show their influence on particle residence time. In-flight particle monitoring system can provide useful information about the velocity and temperature of injected particles in the plasma reactor. The possibility of kinetic limiting step should also be investigated. Injection of carbon donor precursor at different points along the plasma jet with different temperature can shed light to this problem.

The role of sudden temperature drop of plasma jet on the formation of meta-stable phases like austenite was described in chapter 4. This quench phenomenon is the major cause for the formation of other phases (impurities). Focusing on this hypothesis with more experiments can clarify its role and may lead researchers to synthesis of iron carbide particles with less impurities.

References

Alexandrescu, R., Dumitrache, F., Morjan, I., Sandu, I., Savoiu, M., Voicu, I., Fleaca, C. and Piticescu, R. (2004). TiO2 nanosized powders by TiCl4 laser pyrolysis. *Nanotechnology,* vol. 15, n° 5, p. 537-45.

Alexandrescu, R., Morjan, I., Dumitrache, F., Birjega, R., Jaeger, C., Mutschke, H., Soare, I., Gavrila-Florescu, L. and Ciupina, V. (2007). Structural characteristics of Fe3C-based nanomaterials prepared by laser pyrolysis from different gas-phase precursors. *Materials Science and Engineering C,* vol. 27, n° 5-8, p. 1181-1184.

Alexandrescu, R., Morjan, I., Voicu, I., Dumitrache, F., Albu, L., Soare, I. and Prodan, G. (2005). Combining resonant/non-resonant processes: Nanometer-scale iron-based material preparation via CO2 laser pyrolysis. *Applied Surface Science,* vol. 248, n° 1-4, p. 138-146.

Arabczyk, W., Konicki, W., Narkiewicz, U., Jasinska, I. and Kalucki, K. (2004). Kinetics of the iron carbide formation in the reaction of methane with nanocrystalline iron catalyst. *Applied Catalysis A: General,* vol. 266, n° 2, p. 135-145.

Bartholomew, C.H. (1990). Recent technological developments in Fischer-Tropsch catalysis. *Catalysis Letters,* vol. 7, n° 1, p. 303-315.

Boulos, M.I. (1985). The inductively coupled R.F. (radio frequency) plasma. *Pure and Applied Chemistry,* vol. 57, n° 9, p. 1321-1352.

Boulos, M.I. (1991). *Thermal plasma processing.* vol. 19, n°6, p. 1078-1089.

Bouyer, E. (1997a). *Etude de la preparation de poudres et de depots a partir de suspension par plasma inductif: Le cas de l'hydroxyapatite phosphocalcique.* Ph.D., Universite de Sherbrooke (Canada), Canada,

Bouyer, E., Gitzhofer, F., Boulos, M.I., (1997b). Suspension plasma spraying of hydroxyapatite powder preparation by RF plasma. *IEEE Transaction on Plasma Science*, vol. 25, n° 5, p. 1066

Bukur, D.B., Lang, X. and Ding, Y. (1999). Pretreatment effect studies with a precipitated iron Fischer–Tropsch catalyst in a slurry reactor. *Applied Catalysis A: General,* vol. 186, n° 1-2, p. 255-275.

Chang, Y. and Pfender, E. (1987). Thermochemistry of thermal plasma chemical reactions. Part I. General rules for the prediction of products. *Plasma Chemistry and Plasma Processing,* vol. 7, n° 3, p. 275-297.

Cheng, J.P., Zhang, X.B., Yi, G.F., Ye, Y. et Xia, M.S. (2008). Preparation and magnetic properties of iron oxide and carbide nanoparticles in carbon nanotube matrix. *Journal of Alloys and Compounds,* vol. 455, n° 1-2, p. 5-9.

Davis, B.H. Fischer–Tropsch Synthesis: Reaction mechanisms for iron catalysts. *Catalysis Today,* vol. In Press, Corrected Proof,

Davis, B.H. (2003). Fischer-Tropsch synthesis: relationship between iron catalyst composition and process variables. *Catalysis Today,* vol. 84, n° 1-2, p. 83-98.

Dry, M.E. (1996). Practical and theoretical aspects of the catalytic Fischer-Tropsch process. *Applied Catalysis A: General,* vol. 138, n° 2, p. 319-344.

Dry, M.E. (2002). High quality diesel via the Fischer-Tropsch process - a review. *Journal of Chemical Technology & Biotechnology,* vol. 77, n° 1, p. 43-50.

Farhat, S. and Scott, C.D. (2006). Review of the arc process modeling for fullerene and nanotube production. *Journal of Nanoscience and Nanotechnology,* vol. 6, n° 5, p. 1189-210.

Guo, J., Gitzhofer, F. and Boulos, M. (1997). Effects of process parameters on ultrafine SiC synthesis using induction plasmas. *Plasma Chemistry and Plasma Processing,* vol. 17, n° 2, p. 219-249.

Jager, B. and Espinoza, R. (1995). Advances in low temperature Fischer-Tropsch synthesis. *Catalysis Today,* vol. 23, n° 1, p. 17-28.

Jäger, C., Mutschke, H., Huisken, F., Alexandrescu, R., Morjan, I., Dumitrache, F., Barjega, R., Soare, I., David, B. and Schneeweiss, O. (2006). Iron-carbon nanoparticles prepared by CO_2 laser pyrolysis of toluene and iron pentacarbonyl. *Applied Physics A: Materials Science & Processing,* vol. 85, n° 1, p. 53-62.

Jiao, J., Seraphin, S., Wang, X. and Withers, J.C. (1996). Preparation and properties of ferromagnetic carbon-coated Fe, Co, and Ni nanoparticles. *Journal of Applied Physics,* vol. 80, n° 1, p. 103-108.

Kameyama, T., Sakanaka, K., Arakawa, H., Motoe, A., Tsunoda, T. and Fukuda, K. (1993a). Preparation of ultrafine Fe-Si-C powders in a radio-frequency thermal plasma and their catalytic properties. *Journal of Materials Science,* vol. 28, n° 17, p. 4630-4636.

Kameyama, T., Sakanaka, K., Arakawa, H., Motoe, A., Tsunoda, T. and Fukuda, K. (1993b). Preparation of ultrafine Fe-Si-C powders in a radio-frequency thermal plasma and their catalytic properties. *Journal of Materials Science,* vol. 28, n° 17, p. 4630-4636.

Kim, J.H., Kim, J., Park, J.H., Kim, C.K., Yoon, C.S. and Shon, Y. (2007). Synthesis of carbon-encapsulated iron carbide nanoparticles on a polyimide thin film. *Nanotechnology,* n° 11, p. 115609.

Lee, D.W., Yu, J.H., Kim, B.K. and Jang, T.S. (2008). Fabrication of ferromagnetic iron carbide nanoparticles by a chemical vapor condensation process. *Journal of Alloys and Compounds,* vol. 449, n° 1-2, p. 60-64.

Li, S., Krishnamoorthy, S., Li, A., Meitzner, G.D. and Iglesia, E. (2002). Promoted Iron-Based Catalysts for the Fischer–Tropsch Synthesis: Design, Synthesis, Site Densities, and Catalytic Properties. *Journal of Catalysis,* vol. 206, n° 2, p. 202-217.

Montgomery, D. (2001). *Design and Analysis of Experiments.* fifth edition édition, John Wiley & Sons INC.,

Pfender, E. (1999). Thermal Plasma Technology: Where Do We Stand and Where Are We Going? *Plasma Chemistry and Plasma Processing,* vol. 19, n° 1, p. 1-31.

Proulx, P. and Bilodeau, J. (1991). A model for ultrafine powder production in a plasma reactor. *Plasma Chemistry and Plasma Processing,* vol. 11, n° 3, p. 371-386.

Proulx, P., Mostaghimi, J. and Boulos, M.I. (1987). Heating of powders in an r.f. inductively coupled plasma under dense loading conditions. *Plasma Chemistry and Plasma Processing,* vol. 7, n° 1, p. 29-52.

Qiu, J., Li, Q., Wang, Z., Sun, Y. and Zhang, H. (2006). CVD synthesis of coal-gas-derived carbon nanotubes and nanocapsules containing magnetic iron carbide and oxide. *Carbon,* vol. 44, n° 12, p. 2565-2568.

Rahmane, M., Soucy, G. and Boulos, M.I. (1995). Diffusion phenomena of a cold gas in a thermal plasma stream. *Plasma Chemistry and Plasma Processing,* vol. 16, n° 0, p. S169-S189.

Roco, M.C. (1999). Nanoparticles and Nanotechnology Research. *Journal of Nanoparticle Research,* vol. 1, n° 1, p. 1-6.

Sajitha, E.P., Prasad, V., Subramanyam, S.V., Eto, S., Takai, K. and Enoki, T. (2004). Synthesis and characteristics of iron nanoparticles in a carbon matrix along with the catalytic graphitization of amorphous carbon. *Carbon,* vol. 42, n° 14, p. 2815-2820.

Sano, N., Akazawa, H., Kikuchi, T. and Kanki, T. (2003). Separated synthesis of iron-included carbon nanocapsules and nanotubes by pyrolysis of ferrocene in pure hydrogen. *Carbon,* vol. 41, n° 11, p. 2159-2162.

Schulz, H. (1999). Short history and present trends of Fischer–Tropsch synthesis. *Applied Catalysis A: General,* vol. 186, n° 1-2, p. 3-12.

Si, P.Z., Choi, C.J., Brück, E., Geng, D.Y. and Zhang, Z.D. (2005). Structure and magnetic properties of surface alloyed Fe nanocapsules prepared by arc discharge. *Physica B: Condensed Matter,* vol. 369, n° 1-4, p. 215-220.

Smith, R.W., Wei, D. and Apelian, D. (1989a). Thermal plasma materials processingâ€"Applications and opportunities. *Plasma Chemistry and Plasma Processing,* vol. 9, n° 0, p. 135S-165S.

Smith, R.W., Wei, D. and Apelian, D. (1989b). Thermal plasma materials processing Applications and opportunities. *Plasma Chemistry and Plasma Processing,* vol. 9, n° 0, p. 135S-165S.

Song, H. and Chen, X. (2003). Large-scale synthesis of carbon-encapsulated iron carbide nanoparticles by co-carbonization of durene with ferrocene. *Chemical Physics Letters,* vol. 374, n° 3-4, p. 400-404.

Soucy, G., Jurewicz, J.W. and Boulos, M.I. (1995). Parametric study of the plasma synthesis of ultrafine silicon nitride powders. *Journal of Materials Science,* vol. 30, n° 8, p. 2008-2018.

Wang, Z.H., Zhang, Z.D., Choi, C.J. and Kim, B.K. (2003). Structure and magnetic properties of Fe(C) and Co(C) nanocapsules prepared by chemical vapor condensation. *Journal of Alloys and Compounds,* vol. 361, n° 1-2, p. 289-293.

Xiang-Xin Bi, Ganguly, B., Huffman, G.P., Huggins, F.E., Endo, M. and Eklund, P.C. (1993). Nanocrystalline α-Fe, Fe3C, and Fe7C3 produced by CO2 laser pyrolysis. *Journal of Materials Research,* vol. 8, n° 7, p. 1666-74.

Zhang, Z.D., Zheng, J.G., Skorvanek, I., Wen, G.H., Kovac, J., Wang, F.W., Yu, J.L., Li, Z.J., Dong, X.L., Jin, S.R., Liu, W. and Zhang, X.X. (2001). Shell/core structure and magnetic properties of carbon-coated Fe-Co(C) nanocapsules. *Journal of Physics: Condensed Matter,* n° 9, p. 1921.

Zhao, G.Y., Mostaghimi, J. and Boulos, M.I. (1990). The induction plasma chemical reactor: Part II. Kinetic model. *Plasma Chemistry and Plasma Processing,* vol. 10, n° 1, p. 151-166.